The structure and volume of large geysers in Yellowstone National Park, USA and the mineralogy and chemistry of their silica sinter deposits

Dakota M. Churchill [a,b], Michael Manga [a], Shaul Hurwitz [c,*], Sara Peek [b], David E. Damby [c], Richard Conrey [d], John R. Wood [e], R. Blaine McCleskey [f], William E. Keller [g,1], Behnaz Hosseini [g,2], Jefferson D.G. Hungerford [g]

[a] Department of Earth and Planetary Science, University of California, Berkeley, CA, USA
[b] U.S. Geological Survey, California Volcano Observatory, Menlo Park, CA, USA
[c] U.S. Geological Survey, California Volcano Observatory, Moffett Field, CA, USA
[d] Hamilton Analytical Laboratory, Hamilton College, Clinton, NY, USA
[e] National Park Service, Geologic Resources Division, Lakewood, CO, USA
[f] U.S. Geological Survey, Water Mission Area, Boulder, CO, USA
[g] National Park Service, Yellowstone National Park, Wyoming, USA

ARTICLE INFO

ABSTRACT

Siliceous sinter is formed by biogenic and abiogenic opal deposition around hot springs and geysers. Using Structure-from-Motion photogrammetry we generated three-dimensional models of Giant and Castle Geysers from the Upper Geyser Basin of Yellowstone National Park. We use these models to calculate an approximate mass of sinter for each (~2 and ~ 5 kton, respectively) and estimate a range of plausible long-term deposition rates for Castle Geyser (470 to 940 kg·yr^{-1}). We estimate ~2% of the silica discharged from Castle Geyser is deposited as sinter in the cone and proximal terraces. We collected 15 sinter samples following the stratigraphy of each geyser from the older terrace to the younger cone and examined them using a variety of analytical methods. We find that young opaline sinter with high water content (<12 wt% from loss on ignition) contains higher concentrations of major and trace elements, notably As, Sb, Rb, Ga and Cs, relative to older dehydrated sinter. Rare earth element (REE) concentrations in sinter are 2–3 orders of magnitude higher than in the thermal water from which they are deposited. Sinter deposits are enriched in light REE, Gd and Yb when normalized to concentrations in thermal water and enriched in Eu, Tm, and Yb when normalized to the underlying rhyolite. Sinter samples with the highest REE concentrations are also enriched in organic material, implying either microbial uptake of REE, or that organic molecules are efficient ligands that form metal complexes.

© 2021 Elsevier B.V. All rights reserved.

1. Introduction

Geysers are hot springs characterized by intermittent ejection of liquid, water, and steam. Natural geysers are rare, with less than a thousand known worldwide (Bryan, 2018). Most form where recent or active magmatism supplies heat and glacial deposits overlie SiO$_2$-rich rhyolite flows or ignimbrites (Hurwitz and Manga, 2017; Hurwitz et al., 2021). Geyser cones are constructed of geyserite, a type of dense, typically banded or laminated siliceous sinter (opal), commonly with stromatolite-like structures, and is found around geyser vents (Campbell et al., 2015; Jones, 2020). Sinter forms from the precipitation of opal-A from alkaline-chloride thermal waters which become supersaturated with respect to silica (SiO$_2$) upon cooling, steam separation, and evaporation (Lynne, 2012; Campbell et al., 2015; Jones, 2020). Over time, diagenesis transforms the sinter from opal-A to crystalline quartz via dehydration (Herdianita et al., 2000; Lynne and Campbell, 2004; Rodgers et al., 2004; Lynne et al., 2007; Hinman and Kotler, 2013; Liesegang and Tomaschek, 2020).

Characterizing sinter deposits is important for various reasons: They contain microbial biofilms that provide archives of extreme life (Handley et al., 2005; Campbell et al., 2015; Sanchez-Garcia et al., 2019; Sriaporn et al., 2020), they record the highest temperature (~75 to 100 °C) of life (thermophiles) on land (e.g., Braunstein and Lowe, 2001; Campbell et al., 2015), and they have been found in ~3.5 billion-year-old sedimentary deposits in Western Australia, possibly providing clues to the rise of prebiotic molecular systems that have the fundamental properties of life (Djokic et al., 2017; Van Kranendonk et al., 2021a). Sinter deposits are also often spatially related to the structures that

transport hot fluids toward the surface, and they contain traces of precious metals. Therefore, characterization of sinter deposits can provide a guide for geothermal energy and epithermal mineral resource exploration at depth (Cunneen and Sillitoe, 1989; Nicholson, 1989; White et al., 1989; Clark and Williams-Jones, 1990; Brown and Simmons, 2003; Uysal et al., 2011; Sillitoe, 2015; Simmons et al., 2016; Hamilton et al., 2017; Pirajno, 2020). Sinter deposits were also detected on Mars by the *Spirit* rover (Milliken et al., 2008; Squyres et al., 2008; Skok et al., 2010; Ruff and Farmer, 2016; Rapin et al., 2018) with textures that closely resemble those on Earth, and therefore are a key target in the search for ancient Martian life (Cady et al., 2018; Van Kranendonk et al., 2021b).

Approximately half of the world's active geysers occur in the geyser basins of Yellowstone National Park (Bryan, 2018), with the highest concentration in the Upper Geyser Basin (UGB; Fig. 1). Previous studies on silica sinter deposits in Yellowstone's geyser basins have characterized biotic and abiotic controls on their formation and diagenesis (Walter, 1976; Lowe and Braunstein, 2003; Guidry and Chafetz, 2003; Hinman and Walter, 2005; Lynne et al., 2017; Smith et al., 2018), measured the concentrations of select elements and/or isotopic compositions (White et al., 1992; Fournier et al., 1994; Shanks III et al., 2007; Gangidine et al., 2020; Chen et al., 2020), and characterized the chemical and isotopic composition of the alkaline-chloride thermal water from which they are deposited (Fournier, 1989; Hurwitz et al., 2012;

McCleskey et al., 2014; Hurwitz and Lowenstern, 2014; Hurwitz et al., 2016; Cullen et al., 2021). Geologic mapping of the UGB (Muffler et al., 1982) distinguished between old (*osi*) and newer (*si*) sinter units (Fig. 2) based on stratigraphy and outcrop morphology, but without determining absolute ages. However, it was inferred that the geyser cones in Yellowstone post-date the end of the last (Pinedale) deglaciation, 15–14 ka ago, as they would have been removed by glacial erosion (Licciardi and Pierce, 2018). The few radiometric ages of sinter deposits from the UGB suggest nearly continuous deposition throughout the Holocene (Foley, 2006; Lowenstern et al., 2016; Hurwitz et al., 2020). An attempt to date a large number of sinter samples using several radiometric methods confirmed that the deposits are of Holocene age (Churchill et al., 2020).

Despite considerable advances in understanding silica sinter formation in Yellowstone, several key questions remain. For example, how old are some of the largest geyser cones in the UGB (Lowenstern et al., 2016; Churchill et al., 2020)? What are the volumes and deposition rates of these geysers? What are the timescales for polymorphic transformations of silica minerals (from amorphous opal-A to opal-CT to opal-C to quartz)? How do mineralogical and chemical variations correlate with sinter dehydration? Which trace elements are enriched in the sinter compared with the source water? To address these questions, we collected sinter samples from two of the largest active geysers in the UGB, Giant and Castle Geyser (Figs. 1–4) for detailed structural,
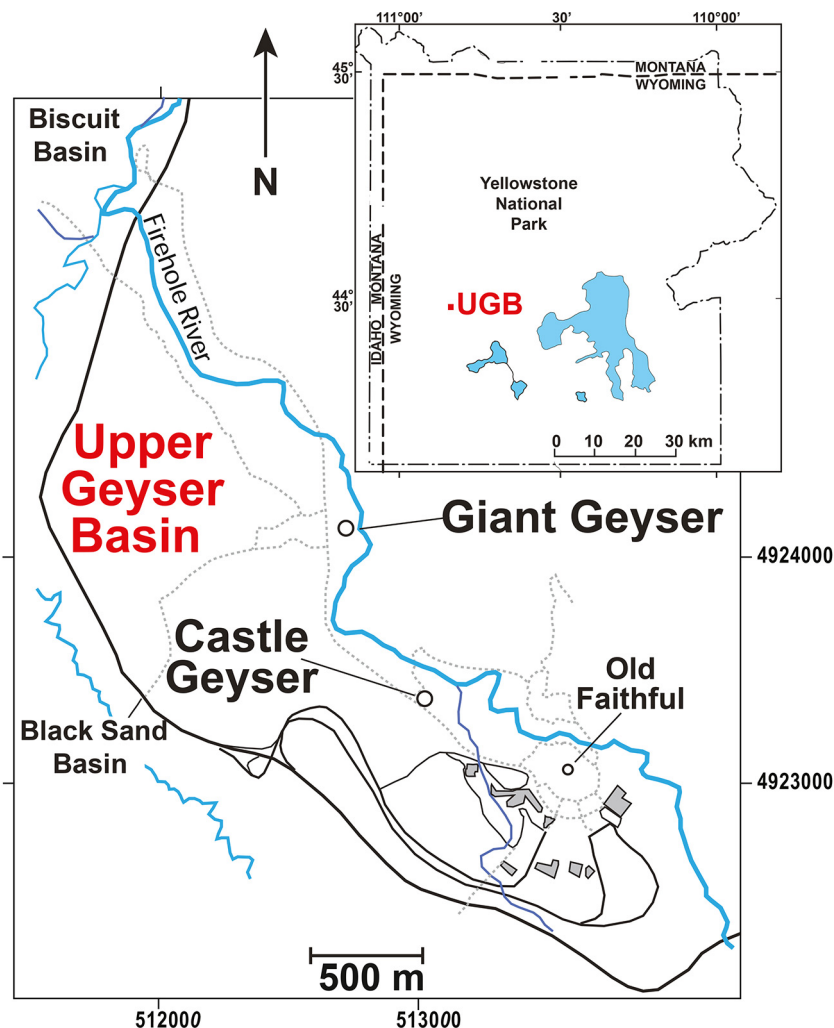
Fig. 1. A map of the Upper Geyser Basin (UGB) with the inset showing a map of Yellowstone National Park. Coordinates for the UGB map are in Universal Transverse Mercator (UTM) Zone 12 N. Gray dashed lines indicate trails and solid black lines indicate roads.
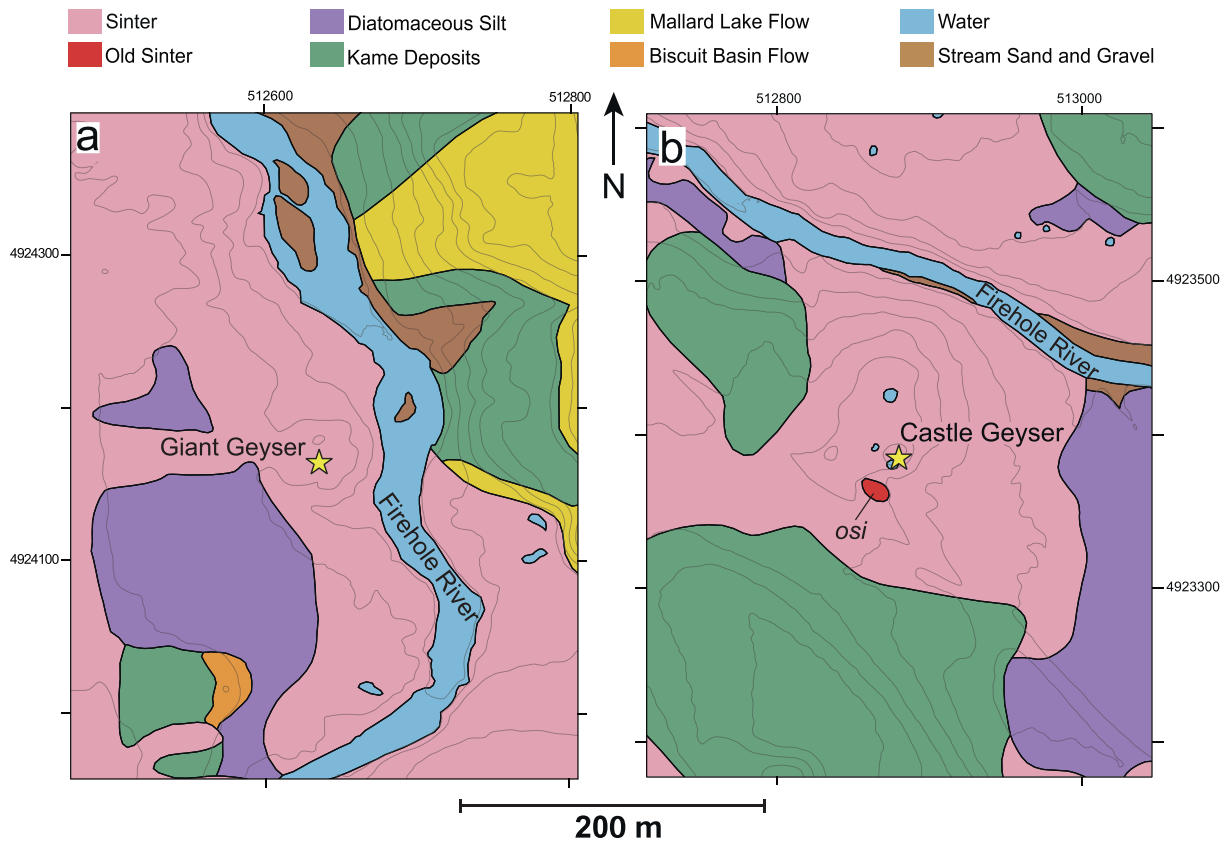
Fig. 2. Geologic maps after Muffler et al. (1982) and digitized by Abedini et al. (2015) for a) Giant Geyser and b) Castle Geyser with the old sinter (*osi*) unit in red mapped on the southwest part of the geyser. Coordinates are in Universal Transverse Mercator (UTM) Zone 12 N. Geyser locations are marked with a star. (For interpretation of the references to colour in this figure legend, the reader is referred to the web version of this article.)

mineralogical, and chemical characterization. Ferdinand V. Hayden who led the 1871 geological survey that resulted in the establishment of Yellowstone as the first U.S. National Park in 1872, wrote about Giant Geyser "*It is readily recognized from its peculiar crater, which has been compared to a broken horn, but, as Stanley says, it is more like the stump of a hollow sycamore tree of gigantic proportions, the top of which has been torn off by a storm*" (Hayden, 1883, p. 195). Hayden wrote that Castle Geyser derived its name "*because of its fancied resemblance to the ruins of a feudal castle, although from most points of view it is more like the ruin of a tower or turret on the end of a platform, suggesting the form of a "monitor iron-clad vessel.*" (Hayden, 1883, p. 204). These early observations reveal a long-standing interest in the structure of geyser cones and, by extension, the mineralogical and chemical controls on their construction.

The main goals of this study were to 1) characterize the size and structure of large geysers in Yellowstone, 2) characterize silica mineral diagenesis and dehydration over time, and 3) characterize the chemical composition of sinter deposits and relate it to the composition of thermal water from which the silica sinter forms. We sampled sinter at the two geysers following the stratigraphy from the older terrace to the younger cone. By sampling along the stratigraphy, we were able to characterize the temporal patterns of sinter mineralogy and chemistry. Addressing the goals of this study can provide a baseline that can serve for future preservation of geysers and other hydrothermal features in Yellowstone National Park (Heasler et al., 2009; Foley et al., 2014). The data and the analysis presented in this study can also inform exploration of geothermal energy and epithermal mineral resources (Hurwitz et al., 2021).

2. Data acquisition and methods of analysis

We generated high-resolution three-dimensional digital reconstructions (models) of Giant and Castle Geysers using structure-from-motion (SfM) photogrammetry (Matthews, 2008). Photographs were taken in a roughly circular path around both geyser cones at evenly spaced camera stations. A total of 52 photos were taken at Castle Geyser in June 2019, and 183 photos were taken at Giant Geyser in April 2020. We used digital single-lens reflex (DSLR) cameras affixed with wide-angle prime lenses (~24 mm) that retained a static or fixed focus, aperture, and ISO settings to ensure consistency of image quality during photography. Precisely known controls (i.e., scale bars) were placed within the area of photography for local scaling. These controls are used to improve size estimations, with scale bar errors of 0.5 mm or better; and increase the fidelity of the generated model. In all cases, a Global Navigation Satellite System (GNSS) capable Global Positioning System (GPS) unit documented the location of the camera and/or scale bar centers. At each photo location, images were taken from approximately one to eight meters in elevation using a telescoping monopod. The models were aligned, calibrated, and georeferenced with AGISoft's photogrammetry software, MetaShape. Models were then exported to CloudCompare, where the surface area and volumes of the sinter cones were estimated as a solid object.

Six sinter samples were collected from Giant Geyser (Fig. 4a,b) and nine samples were collected from Castle Geyser (Fig. 4c,d) in April 2018. Details of the methods used for collecting, processing, and analyzing the samples are found in Churchill et al. (2021). Here we provide a condensed summary. At each geyser, approximately fist-sized samples
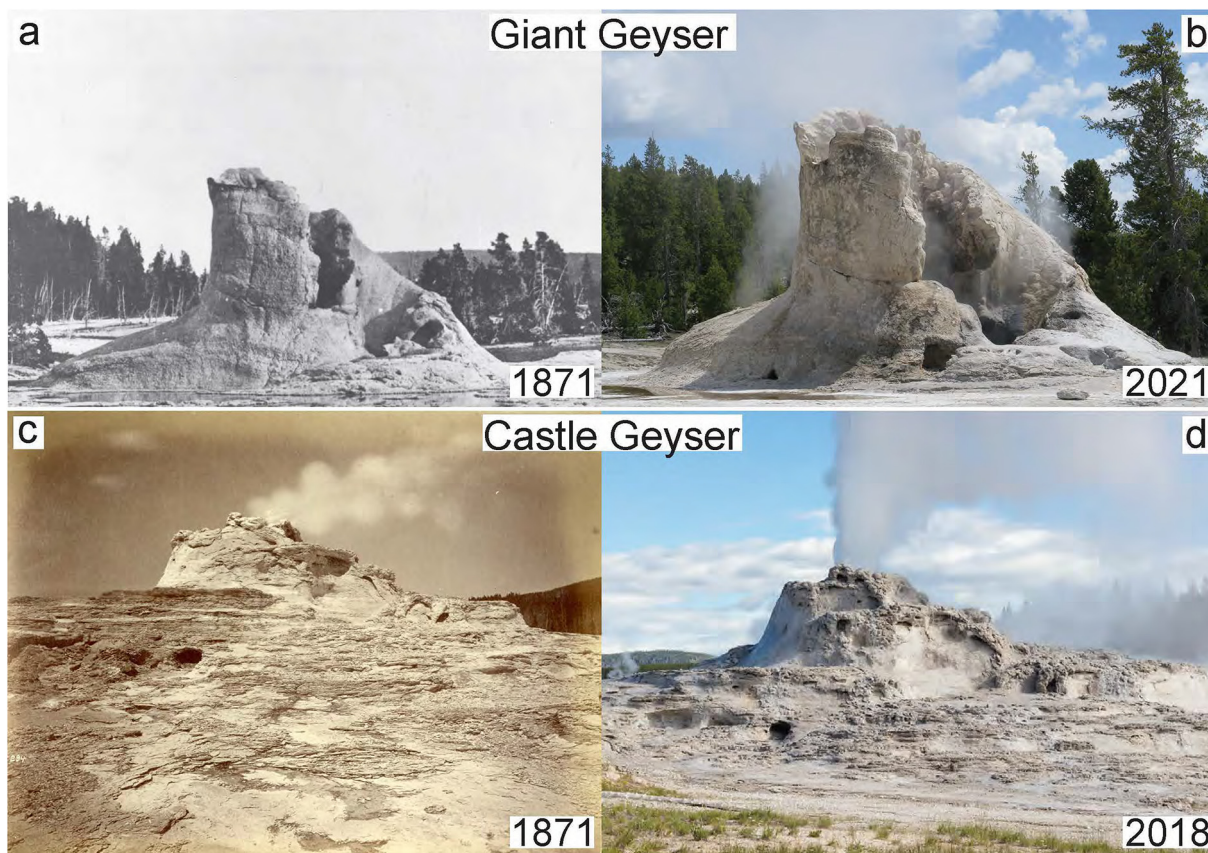
Fig. 3. Comparison of photos from Giant and Castle Geysers separated by almost 150 years. a) Photo of Giant Geyser from 1871 (U.S. Geological Survey Denver Library Photographic Collection, Jackson, W.H. Collection). b) Photo of Giant Geyser from 2021 to 05–17 (Megan Norr, National Park Service). c) Photo of Castle Geyser from 1871 (U.S. Geological Survey Denver Library Photographic Collection, Jackson, W.H. Collection). d) Photo of Castle Geyser from 2018 to 07–01 (Jacob W. Frank, National Park Service).

were collected and labeled sequentially from the shield (oldest) to the top (youngest) of the cone (Table 1, Fig. 4). Six samples collected at Castle Geyser (Fig. 4c,d) are from the cone, a unit mapped as *si*, and three are from the shield, a unit mapped as *osi* (Fig. 2b). The stratigraphic relationship between the three *osi* (old sinter) samples could not be determined.

Thin sections for each sample were examined under a polarizing microscope to identify micro- to millimeter-scale sinter textures and any accessory minerals or lithic components. Mineral phases and microscale morphologies were identified using X-ray powder diffraction (XRPD), scanning electron microscopy (SEM), and energy dispersive X-ray spectroscopy (EDS) at the U.S. Geological Survey laboratories in Menlo Park, California. To provide a crude indication of the state of the opal structure in each sinter sample, Full-Width Half-Maximum (FWHM) values were manually calculated by fitting a curve and base line to the XRPD spectra (Herdianita et al., 2000; Lynne and Campbell, 2004; Liesegang and Tomaschek, 2020).

Samples were analyzed for major and trace element concentrations using a Thermo ARL Perform'X X-ray fluorescence (XRF) spectrometer at the Hamilton Analytical Laboratory at Hamilton College, New York, following protocols described in Johnson et al. (1999). Uncertainties in the XRF determinations depend upon element concentration and range from approximately 0.2% for SiO_2 to <10% for trace elements such as Ga and Cs. Samples were further analyzed for trace element concentrations (including Rare Earth Elements - REE) using Laser Ablation Inductively Coupled Plasma Mass Spectrometry (LA-ICP-MS) at the Colorado School of Mines, Colorado. In the calculations and figures presented in this paper we use concentrations determined by XRF analysis for SiO_2, Ga, Cs, Na and K, and all other trace element concentrations (including As, Ge and Sb) are reported from LA-ICP-MS

analysis. The weight percent change using loss on ignition (LOI) was determined by heating the powdered samples to 900 °C in SiO_2 crucibles. These measurements are reproducible to ~10%.

3. Results

3.1. Structure and mass of Giant and Castle Geysers

The three-dimensional models of Giant and Castle Geysers include both their cones and underlying shields (Fig. 5) and can be found online at https://irma.nps.gov/DataStore/Reference/Profile/2273777 and https://irma.nps.gov/DataStore/Reference/Profile/2278667. At both geysers, layering and stratification at millimeter to meter scales is visible due to variations in sinter colour and texture. The model of the Giant Geyser complex includes the neighboring and smaller Bijou, Catfish, Mastiff, and Turtle Geysers (Fig. 5b), which sometimes erupt along with Giant Geyser. Giant Geyser's cone rises approximately 4 m above the relatively flat platform (Fig. 5a), is 6 m wide at its base, and gradually narrows to 3 m at its top. The structure of Giant Geyser's cone is relatively cylindrical, and its western side is open, revealing rougher sinter textures on the inside of the cone compared to the exterior. In contrast, the Castle Geyser cone is a 5 m tall asymmetrical structure with a 1 m orifice from which water erupts (Fig. 5c). The slope of the northern side of the cone is steep relative to the southern side, where multiple terraces accumulate small pools of erupted water. The base of the cone is 26 m at its widest and 16 m at its narrowest, for an estimated area of 416 m^2. Bright orange bacterial mats grow along Castle Geyser's southern shield.

The estimated volumes of Giant Geyser complex and Castle Geyser cone are ~2500 m^3 and ~ 6060 m^3, respectively. Assuming a maximum
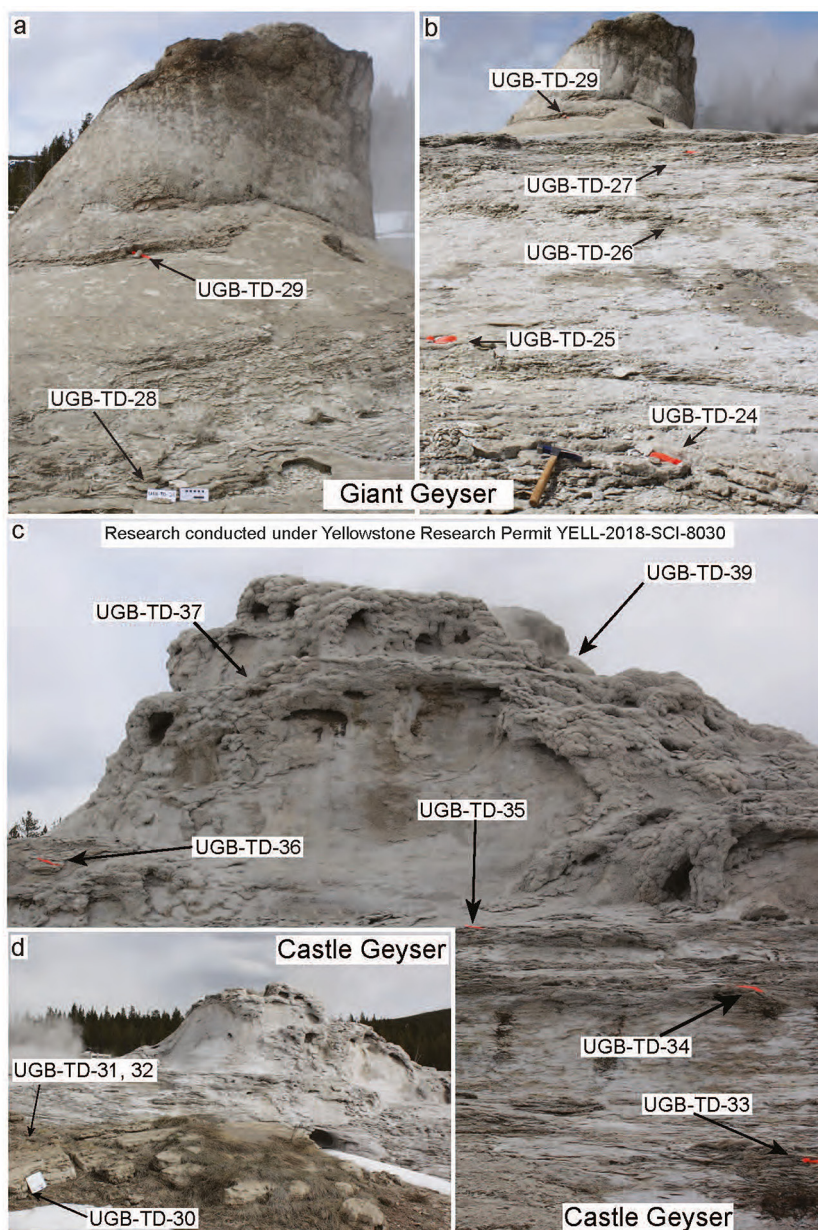
Fig. 4. Photos of Giant and Castle Geysers with labels indicating sample locations. a) and b) View of Giant Geyser looking to the west. c) Photo of Castle Geyser looking to the southeast. d) Photo looking to the northeast showing the Castle Geyser shield within an area mapped as old sinter (*osi;* Muffler et al., 1982). Samples were collected under Research Permit YELL-2018-SCI-8030.

sinter porosity of 60% (Munoz-Saez et al., 2016), the minimum calculated volumes of sinter which compose the Giant Geyser complex and Castle Geyser's cone are ~1000 m^3 and ~ 2400 m^3, respectively. If we model the geyser conduit as a cylinder with a radius of 1 m and a height of 5 m, then the calculated volumes only decrease by ~8 m^3. Sinter at Giant Geyser consists mainly of opal-A with a density of 2180 kg·m^{-3} (Munoz-Saez et al., 2016), and smaller amounts of slightly denser cristobalite and quartz, both with a density of 2650 kg·m^{-3}. Thus, we approximate the overall sinter density at Giant Geyser to be ~2300 kg·m^{-3} and calculate a mass of ~2 kton. The calculated mass of Castle Geyser's cone, which sampling suggests is composed entirely of opal-A (Table 1) is ~5 kton. With all the approximations included in these calculations (volume, porosity, voids and density), we estimate an uncertainty of 20% in these calculations of sinter mass.

3.2. Sinter texture, morphology, mineralogy, and water content

All the mineralogical and chemical data associated with the analysis of sinter samples from Giant and Castle Geysers are available in Churchill et al. (2021). Samples collected near the geyser orifice (UGB-TD-29 from Giant Geyser and UGB-TD-37 and TD-39 from Castle Geyser) display cauliflower texture on their exterior surface (Fig. 6a,b), with a filamentous geyserite interior texture (Fig. 6c). Some samples preserve millimeter-scale parallel layering (UGB-TD-27; Fig. 6d). Sinter texture changes with increasing age (Fig. 6e). On a smaller scale, samples with amorphous opal-A to opal-A/C display botryoidal, bumpy, or clustered micro-spheres (Fig. 7a,b), which sometimes form on organic features such as microbial filaments (Fig. 7c) and mats (Fig. 7d), or pollen (Fig. 7e). Some layers of silicified microbial mats are found

Table 1
Mineralogy and water content of samples from Giant and Castle Geysers.

Sample ID	Minerals[a]	Quartz[b] %	FWHM[c]	LOI[d] wt%
Giant Geyser				
UGB-TD-24	Opal-C + Quartz	<5	0.8	2.7
UGB-TD-25	Opal-C + Quartz	<10	0.8	2.2
UGB-TD-26	Opal-A/C	<1	4.4	3.9
UGB-TD-27	Opal-A/C	<1	4.9	6.8
UGB-TD-28	Opal-C/A + Quartz	<5	1.4	6.7
UGB-TD-29	Opal-A/C	<1	5.1	9.6
Castle Geyser				
UGB-TD-30[e]	Opal-A/C	<2	5.5	4.5
UGB-TD-31[e,f]	Opal-CT + Quartz	2	2.7	24
UGB-TD-32[e]	Opal-A/C	0	4.0	5.8
UGB-TD-33	Opal-A	<2	6.3	8.9
UGB-TD-34	Opal-A	<1	6.5	9.6
UGB-TD-35	Opal-A	<2	6.0	8.7
UGB-TD-36	Opal-A	<1	6.3	9.2
UGB-TD-37	Opal-A	<1	6.1	10
UGB-TD-39	Opal-A	0	6.4	12

[a] Detected with X-ray powder diffraction (XRPD).
[b] Visually estimated from representative thin sections.
[c] Full-Width Half-Maximum; a crude indication of the state of the opal structure.
[d] Loss on Ignition. The value is considered as a proxy for water content.
[e] From unit mapped as old sinter (*osi*; Muffler et al., 1982).
[f] High concentration of organic matter.

alternating with SiO_2-rich layers (Fig. 7d). Significant amounts of silicified organic material are visible on a micrometer scale in samples UGB-TD-26, −28, −30, −31 and − 32. Samples that are more diagenetically mature (UGB-TD-24 from Giant Geyser) display a denser micrometer-scale morphology, with crystalline silica polymorphs (quartz) lining and filling pores (Fig. 7f).

The XRPD spectra of samples from Giant and Castle Geysers are shown in Fig. 8 and the identified minerals are summarized in Table 1. Even though the silica polymorphs opal, cristobalite (C), tridymite (T), and quartz (Q) were the only minerals identified by XRPD, petrographic and SEM-EDS analysis reveal sub-millimeter feldspar, calcite, halite, and iron oxides. These accessory minerals, or other undetected chemical impurities, are the likely cause for any white, brown, and gray colour variations (Fig. 6) visible in the sinter at both Giant and Castle Geysers.

Sinter samples UGB-TD-24 and UGB-TD-25 from the top of Giant Geyser consist of opal-C and quartz with FWHM values of 0.8° 2θ (Table 1). UGB-TD-26, UGB-TD-27, and UGB-TD-29 consist of opal-A/C with FWHM values ranging from of 4.4° to 5.1° 2θ. Sample UGB-TD-28 consists of opal-A/C and quartz with a FWHM of 1.4° 2θ. At Castle Geyser, samples from the cone (*si*; UGB-TD-33−39) consist entirely of opal-A with FWHM values of ~6° 2θ, whereas samples from the shield (*osi*; UGB-TD-30-32) consist of opal-A/C, opal-CT and quartz with FWHM values ranging between 2.7° and 5.5° 2θ.

Loss on ignition (LOI) is typically considered as a proxy for water concentration as molecular water and structural silanol (a functional group with Si–O–H connectivity) in the sinter (Jones and Renaut, 2004; Day and Jones, 2008). However, the LOI value could include other volatile components (CO_2, F, Cl, S, and organics) that we did not measure directly. Anomalously high LOI values, such as measured for sample UGB-TD-31 (~24%), likely results from high concentrations of organic material. At Giant Geyser, LOI decreases from 9.6% at the top of the cone (UGB-TD-29) to 2.2% near the base of the cone (UGB-TD-25; Table 1). At Castle Geyser, the LOI decreases from 12.0% at the top of the cone (UGB-TD-39) to 4.5% on the shield (UGB-TD-30).

3.3. Sinter chemistry

Silica (SiO_2) concentrations increase with increasing age from 88.9 wt% (UGB-TD-29) to 96.8 wt% (UGB-TD-24) at Giant Geyser (Fig. 9a), and from 84.5 wt% (UGB-TD-39) to 94.1 wt% (UGB-TD-30) at Castle Geyser (Fig. 10a). Of the other major oxides, Na_2O has the highest concentrations, and at both geysers its concentration decreases with increasing age (Figs. 9b and 10b). The concentrations of Al_2O_3, MnO, CaO, and K_2O also decrease with increasing sinter age, whereas the concentrations of TiO_2, FeO, MgO, and P_2O_5 remain relatively consistent.

The trace elements with the highest concentrations in the sinter samples are Ga and Sb (both with >750 ppm, although concentrations in most samples are much lower), Cs (>250 ppm), and As and Rb (both with >25 ppm). Concentrations of Ba, Cu, and Zn are >10 ppm, and concentrations of Cr, Ge, Ni, Pb, Sr, V, and Zr are >1 ppm. All other measured trace elements have concentrations >1 ppb except for Cr and Ni in sample UGB-TD-32, where concentrations are below the LA-ICP-MS analytical detection limits. At both geysers, concentrations of
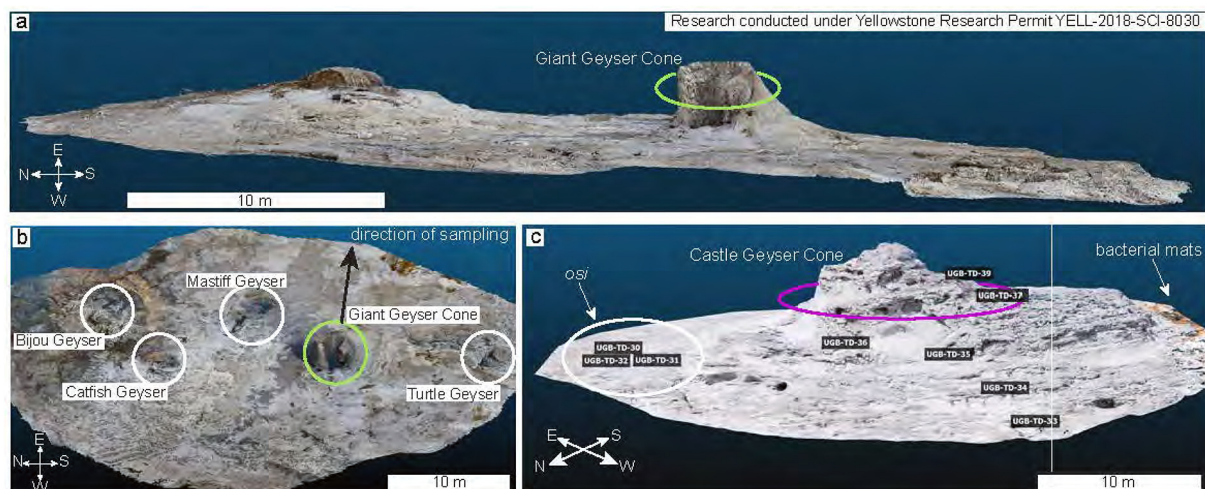
Fig. 5. a) Three-dimensional model of the Giant Geyser complex using Structure-from-Motion (SfM) photogrammetry looking toward the east. Steam interference led to the top of the cone being cut during image processing. b) Three-dimensional model of the Giant Geyser complex from an aerial view. From left to right, the complex includes Bijou Geyser, Catfish Geyser, Mastiff Geyser, Giant Geyser (circled in green), and Turtle Geyser. Samples were collected moving from Giant Geyser cone toward the east. c) Three-dimensional model of Castle Geyser created using Structure-from-Motion photogrammetry. The cone is circled in magenta. The locations of samples collected are draped on the model looking to the southeast. Samples UGB-TD-30, −31, −32 on the left side of the model were collected from an area mapped as old sinter (unit *osi*; Muffler et al., 1982). Samples were collected under Research Permit YELL-2018-SCI-8030. (For interpretation of the references to colour in this figure legend, the reader is referred to the web version of this article.)
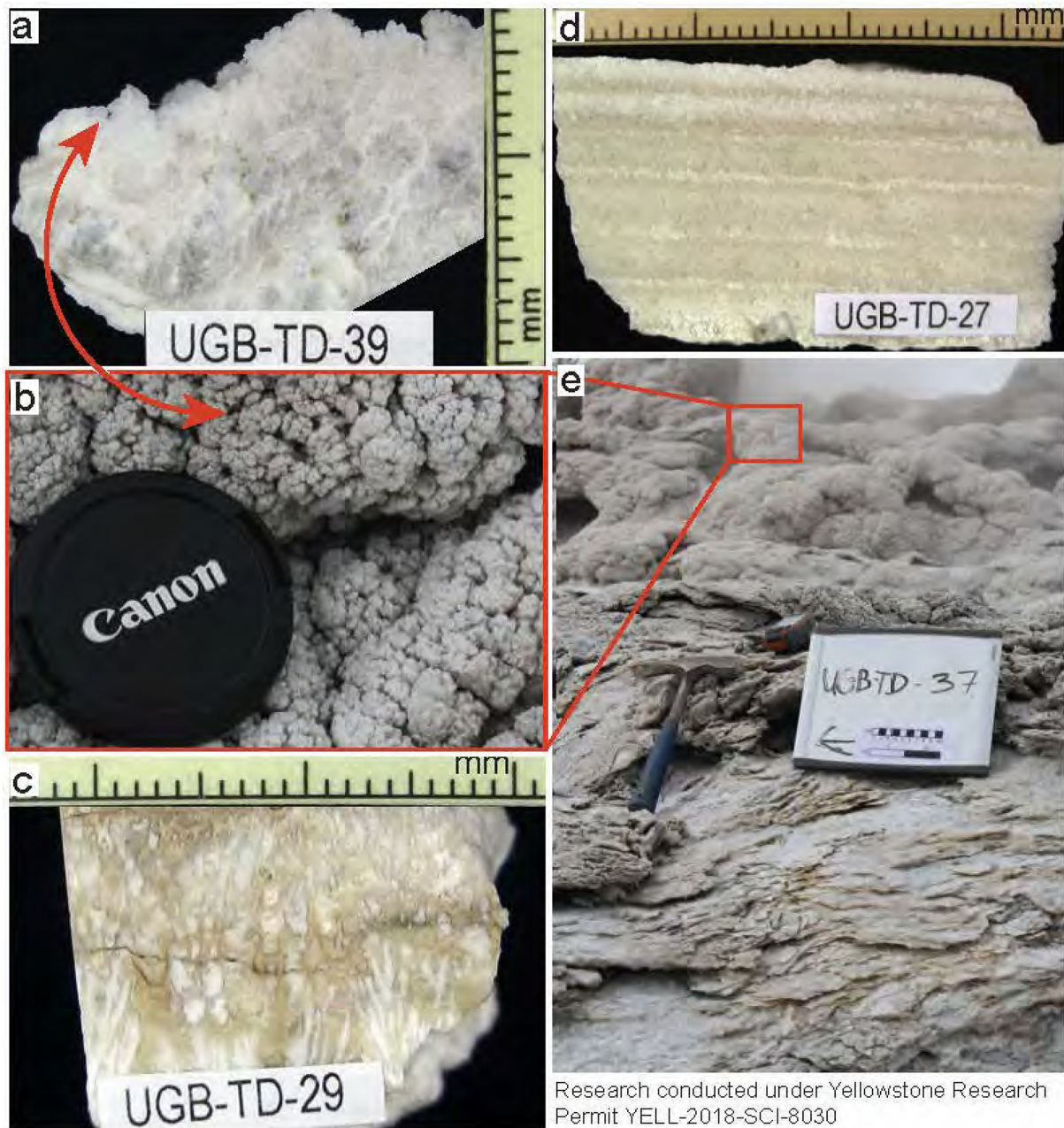
Fig. 6. Photos of sinter samples exhibiting a variety of textures. a) Mottled interior with an exterior cauliflower texture. b) Cauliflower texture collected from sinter samples immediately next to the geyser orifice (i.e. UGB-TD-39). c) Interior filamentous texture. d) Finely laminated palisade texture. e) Texture change along stratigraphy at Castle Geyser. Research was conducted under Yellowstone Research Permit YELL-2018-SCI-8030.

Ag, As, Cs, Ga, Rb, Sb, Sr, and Tl generally decrease with increasing sinter age (Figs. 9c,d, and 10c,d) and the concentration of Sc increases with increasing sinter age.

Major and trace element concentrations, including REE, in sample UGB-TD-31 are anomalous because of high organic material content (high LOI). Excluding UGB-TD-31, REE concentrations from both geysers range from 0.6 ppb to 4.4 ppm. Samples UGB-TD-26 and -28 have the highest REE concentrations at Giant Geyser, and samples UGB-TD-31 and -32 have the highest concentrations at Castle Geyser. The concentrations of REEs at Giant Geyser or along Castle Geyser's cone (*si* unit) do not correlate with increasing sinter age; however, sinter from Castle Geyser's shield (*osi* unit) has higher REE concentrations than sinter from the cone. When sinter REE concentrations are normalized to those of the thermal water from the Giant Geyser outflow (sample

09WA157 in McCleskey et al., 2014), there is a slight negative Eu anomaly, positive Gd and Yb anomalies, and the light REE (LREE) are enriched by up to 100 times compared to the heavy REE (HREE) (Fig. 11a,c). When normalized to the underlying rhyolite (Biscuit Basin flow), Eu, Tm and Yb are enriched (Fig. 11b,d).

4. Discussion

4.1. Geyser cone construction and sinter deposition rates

Although our attempt to date the sinter samples using radiometric methods was mostly unsuccessful, U-series analyses of four samples yielded ages between 2.2 ± 7.9 ka (UGB-TD-39) and 7.4 ± 6.3 ka (UGB-TD-27) (Churchill et al., 2020). Furthermore, Lodgepole Pine
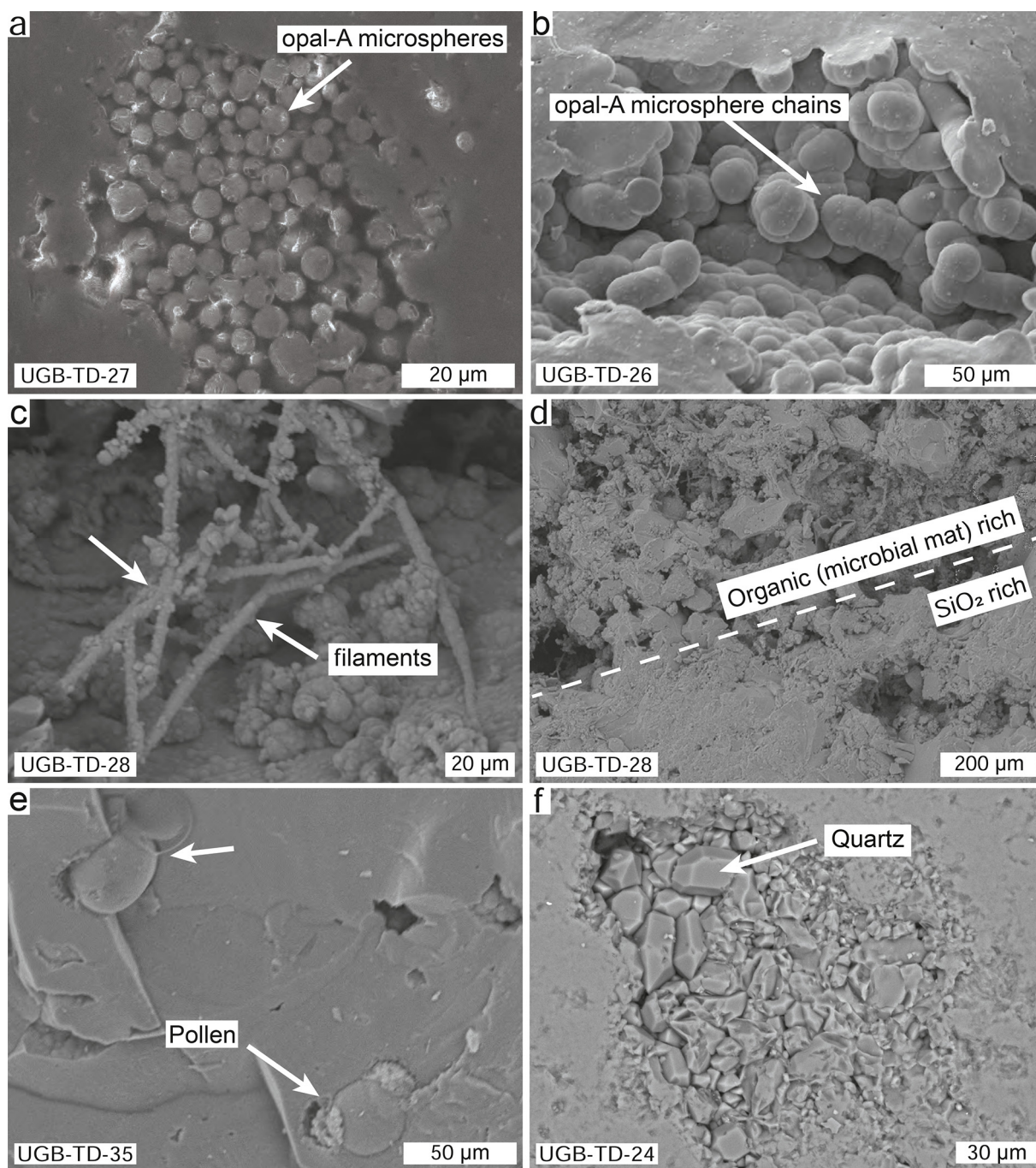
Fig. 7. Representative scanning electron micrographs of samples from Giant and Castle Geysers. a) Thin-section cut revealing opal-A microspheres of ~5 μm diameter. b) Chains of opal-A microspheres with diameters of ~20 μm in pore space of a rough sample mount. c) Silicified filaments with incipient coating by opal-A microspheres visible in a rough mount. d) Contact between layers of silicified microbial material layer and inorganic silica layers on the exterior of a rough mount. e) Silicified pollen grains in a matrix of botryoidal, coalesced opal-A microspheres. f) Thin section image of microcrystalline quartz filling in a pore space.

(*Pinus contorta*) is the dominant pollen in samples UGB-TD-31 and UGB-TD-32 from the base of Castle Geyser (*osi* unit), implying that geyser construction began after ~11 ka BP (Christopher Schiller, Montana State University, written communication, October 2019). Photo comparison of Giant and Castle Geyser from 1871 with photos taken in 2018 and 2021 suggest very little change in their structures over almost 150 years (Fig. 3), thus we infer that construction of large geyser cones occurs over millennial timescales. This supposition is supported by observations from Old Faithful Geyser (Fig. 1) where, during a severe drought in the mid-13th to mid-14th centuries, trees grew on high parts of the mound, implying that at that time the mound closely resembled its current appearance. Thus, to create the present mound, Old Faithful Geyser was likely erupting for millennia prior to tree growth (Hurwitz et al., 2020).

To calculate plausible long-term average sinter deposition rates, we divide the mass of the Castle Geyser cone (~5 kton) by the maximum plausible age (11 ka). This approach results in a minimum net deposition rate of ~470 kg·yr^{-1}. Plausibly, the geyser could be half as old (5500 years), which would result in double the deposition rate (~940 kg·yr^{-1}). These calculated rates have large uncertainties, because they do not account for erosion, or climate variations that control deposition rates through water discharge, air temperature, and evaporation.
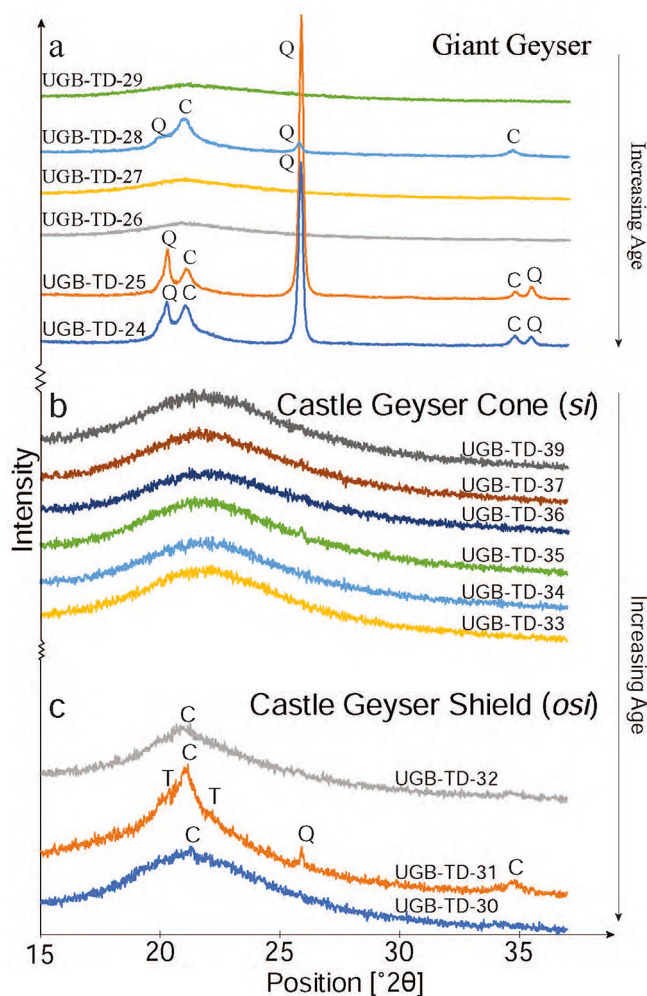
Fig. 8. X-ray powder diffraction (XRPD) spectra of samples from a) Giant Geyser, b) Castle Geyser's cone and c) Castle Geyser's shield (unit *osi*; Muffler et al., 1982). Spectra are arranged according to stratigraphic position with the younger samples at the top of each panel. The broad peak from ~15° to 30° 2θ identifies opal. Letters next to spectral peaks correspond to quartz (Q), cristobalite (C), and tridymite (T).

For example, Castle Geyser likely was dormant during the same period of severe drought that ceased Old Faithful Geyser's eruptions (Hurwitz et al., 2020). Despite the large uncertainties associated with the calculated long-term sinter deposition rates at Castle Geyser, they are within the same order of magnitude as the rates calculated using other methods and for shorter periods of time (Table 3).

The silica deposited as opal is probably a small fraction of the silica transported by water discharged from eruption of the geysers. Water discharge was not measured at either Giant or Castle Geysers, but it was measured in September 2010 at Lone Star Geyser, a large cone geyser with approximately the same structure and volume, located ~5 km south-southeast from Giant and Castle Geysers (Karlstrom et al., 2013). Water discharge and SiO_2 concentration at Lone Star Geyser were ~62,000 $m^3 \cdot yr^{-1}$ and 330 $mg \cdot l^{-1}$ for an annual SiO_2 discharge of ~20,000 kg. By assuming that silica discharge rates at Castle and Lone Star Geysers are similar, we infer that the maximum plausible long-term silica deposition rate in the cone and on the terrace is ~2% of the total silica discharge from Castle Geyser.

4.2. Mineralogic maturation and dehydration

As sinter deposits mature, they dehydrate and the silica minerals transform gradually from opal-A to quartz (Herdianita et al., 2000; Lynne et al., 2007). The sinter deposits from both Giant and Castle

Geysers follow this trend of increasing maturation with increasing age. The younger samples from Giant Geyser consist of opal-A and opal-A/C microspheres and have lower structural order and higher concentrations of water compared to the older samples. The anomalous mineralogy and elevated water content of sample UGB-TD-28 (LOI of 6.7 wt%) is likely a result of being out of stratigraphic order (Fig. 4a). Interestingly, samples UGB-TD-25 and -24 from the base of Giant Geyser have 2.7 and 2.2 wt% LOI respectively, which is slightly higher than the concentration of H_2O measured nearly 140 years earlier (1.5 wt% H_2O) on a sample collected from approximately the same location by the Hayden Expedition (Hayden, 1883, p. 415). Samples UGB-TD-25 and -24 are also the only two samples with significant amounts of quartz (Table 1).

In contrast to the mineralogical maturation pattern at Giant Geyser, a difference in maturation state at Castle Geyser is only found between the *si* units on the cone and the *osi* units on the shield. All samples from Castle Geyser's cone are composed of immature botryoidal, coalesced microspheres of opal-A with low structural order (FWHM ~6.3 2θ) and high amounts of water (>8.9 wt%). The older sinter deposits from the shield of Castle Geyser (*osi* unit; Muffler et al., 1982) contain more mature SiO_2 polymorphs, less water (<5.8 wt%), and exhibit higher structural order (FWHM <5.5 2θ).

The silica maturation and sinter dehydration at Giant and Castle Geyser match trends noted in previous studies (Lynne et al., 2007). Without absolute age constraints, the duration of these transformations cannot be determined. Because both geysers are of Holocene age, the rates of mineral transformations in their deposits differ from previously inferred rates that suggested it takes several thousand years to transform opal-A to opal-CT and opal-C, and tens of thousands of years for transformation to microcrystalline quartz (Rodgers et al., 2004). Nevertheless, the post-depositional environment of sinter, including the presence of organic matter, could accelerate the maturation process (Herdianita et al., 2000; Jones and Renaut, 2003; Lynne et al., 2007; Rodgers et al., 2004).

4.3. Major and trace element enrichment in sinter

The alkaline-chloride thermal waters in the central part of the UGB where Giant and Castle Geysers are located typically have pH values of 7.5 to 9.0 and SiO_2, Cl^-, SO_4^{2-}, Na^+ and K^+ concentrations of 280–350 $mg \cdot l^{-1}$, 300–500 $mg \cdot l^{-1}$, 15–20 $mg \cdot l^{-1}$, 300–450 $mg \cdot l^{-1}$ and 15–20 $mg \cdot l^{-1}$, respectively (Hurwitz et al., 2012, 2016; McCleskey et al., 2014; Cullen et al., 2021). The concentration of HCO_3^- varies substantially across the basin, inferred to result from variations in reservoir temperature (Fournier, 1989). Concentrations of As and Sb are about 1.5 $mg \cdot l^{-1}$ and 80–140 $\mu g \cdot l^{-1}$, respectively. The major solutes in the thermal waters are derived from leaching, mostly at temperatures of 175–275 °C (Cullen et al., 2019), of the underlying rhyolite, which erupted after the formation of the 0.631 Ma Yellowstone Caldera (Christiansen, 2001; Matthews et al., 2015).

The concentrations of SiO_2 (>84.5 wt%), other major oxides with concentrations of 0.1–0.4 wt% (Na_2O, K_2O and Al_2O_3), trace elements with concentrations of >100 ppm (Ga, Cs, Sb) and trace elements with concentrations of 1–100 ppm (As, Ba, Cr, Cu, Ge, Ni, Pb, Rb, Sr, V, Zn, Zr) in the geyserite at Giant and Castle Geysers are mostly similar to those in siliceous sinter deposited in other hydrothermal areas (McKenzie et al., 2001; Brown and Simmons, 2003; Uysal et al., 2011; Simmons et al., 2016; Sanchez-Yanez et al., 2017; Campbell et al., 2018). Concentrations of Ag and Au (2–19 ppb) in sinter deposits from Yellowstone were previously measured by White et al. (1992) and Fournier et al. (1994). The highest concentrations of Ag are in the youngest samples from Castle Geyser (UGB-TD-37, −39), 218 and 215 ppb, respectively, whereas the old sinter samples contain 22–44 ppb (Churchill et al., 2021). The concentration of Ag in sinter from Giant Geyser ranges between 4 and 22 ppb. We did not measure the concentration of Au in this study.
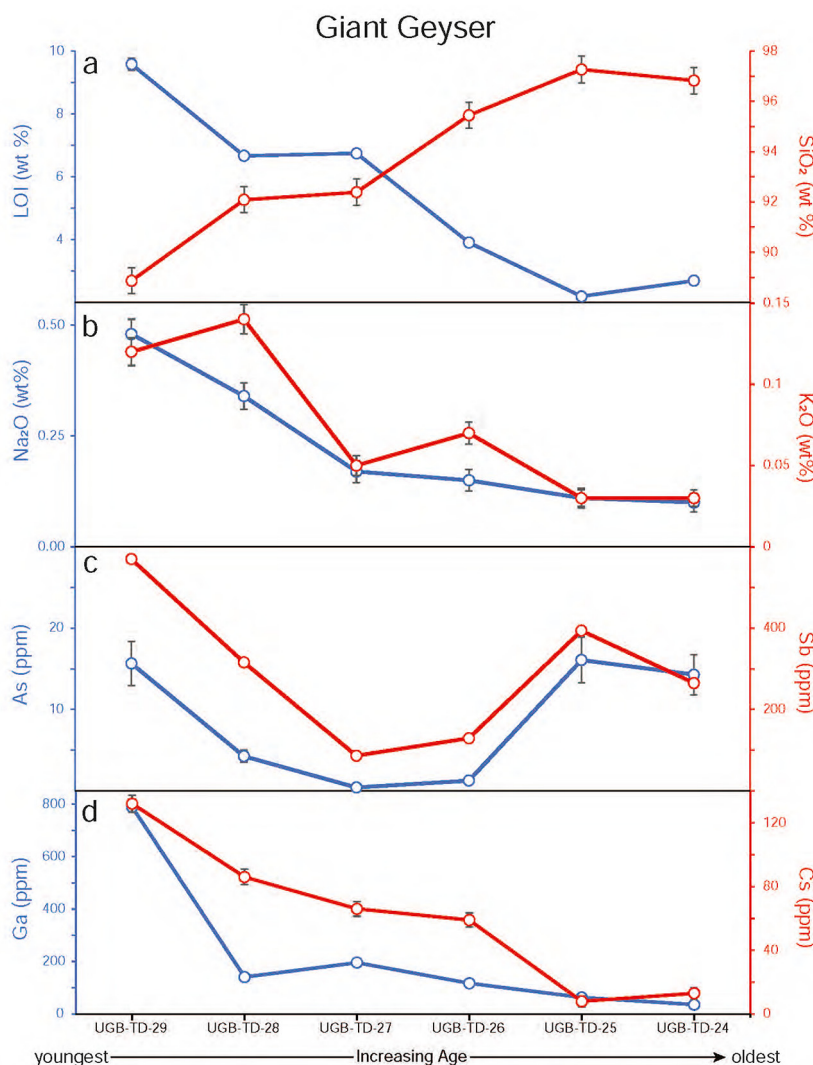
Fig. 9. Concentrations as a function of stratigraphic position at Giant Geyser. The age of samples increases to the right. a) Loss on ignition (LOI; interpreted as water percentage) (blue symbols and curve) and SiO_2 (red symbols and curve). b) Concentration of Na (blue symbols and curve) and K (red symbols and curve). c) Arsenic (As; blue symbols and curve) and antimony (Sb; red symbols and curve) concentrations. d) Gallium (Ga; blue symbols and curve) and cesium (Cs; red symbols and curve) concentrations. Data are tabulated in Churchill et al. (2021). Blue symbols and curves relate to the left Y-axes and red symbols and curves relate to the right Y-axes. Error bars are shown with 2-sigma (95%) confidence. If error bars are not visible it is because they are smaller than the symbols. (For interpretation of the references to colour in this figure legend, the reader is referred to the web version of this article.)

Many of the metals and metalloids found in these sinters with elevated concentrations (i.e., Ga, Sb, Yb, Gd) are in high demand due to their growing usage in a wide range of applications including in telecommunications, green energy, and medical devices (Graedel et al., 2015; White and Shine, 2016; Schulz et al., 2017; Månberger and Johansson, 2019). Additionally, elevated concentrations of As and Sb could be toxic in aquatic food chains (Filella et al., 2009; Bowell et al., 2014).

It is generally understood that the incorporation of elements other than silicon into sinter occurs through isomorphous substitution into, and adsorption onto, silica surfaces and accessory minerals (Pope et al., 2005; Kaasalainen and Stefánsson, 2012; Sanchez-Yanez et al., 2017), and through association with adsorbed water and/or surface silanol groups (Jones and Renaut, 2003; Rodgers et al., 2004). The youngest samples from the two geysers, sample UGB-TD-29 (Giant Geyser) contains 88.9 wt% SiO_2 and 9.6 wt% LOI and sample UGB-TD-39 (Castle Geyser) contains 84.5 wt% SiO_2 and 12 wt% LOI. Thus, element enrichment is likely a result of either incorporation into the opal structure or association with the water.

Despite the significance of quantifying trace element partitioning between sinter and the thermal water from which they are deposited,

only a few studies have done so. Most focused on the partitioning of As and B (Ellis and Sewell, 1963; Ichikuni, 1968; Ballantyne and Moore, 1988; McKenzie et al., 2001), Al and Fe (Ichikuni, 1970) and REE elements (Feng et al., 2014). To calculate enrichment of various elements in the sinter, we defined a partition coefficient K_D for pairs of element ratios in the sinter over the same ratio in the thermal water from which the opal was deposited:

$$K_D = \frac{X/x_{Sinter}}{X/x_{water}} \qquad (1)$$

where X is the molar concentration of the larger atom and x is the molar concentration of the smaller atom in the same column of the periodic table. We determine K_D for pairs of elements that are typically enriched in thermal waters (Table 2); K/Na, Ge/Si and Ga/Al are ratios of elements from the IV period over elements from the III period, Sb/As (V over IV period) and Cs/Rb (VI over V period). There are insufficient concentration data from thermal water in the UGB to determine K_D for other relevant element pairs such as Cd/Zn, and Zr/Ti. Our approach for defining element enrichment in the sinter differs from that of McKenzie et al. (2001) that normalized trace metal (As, Sb, B, Tl and Hg)
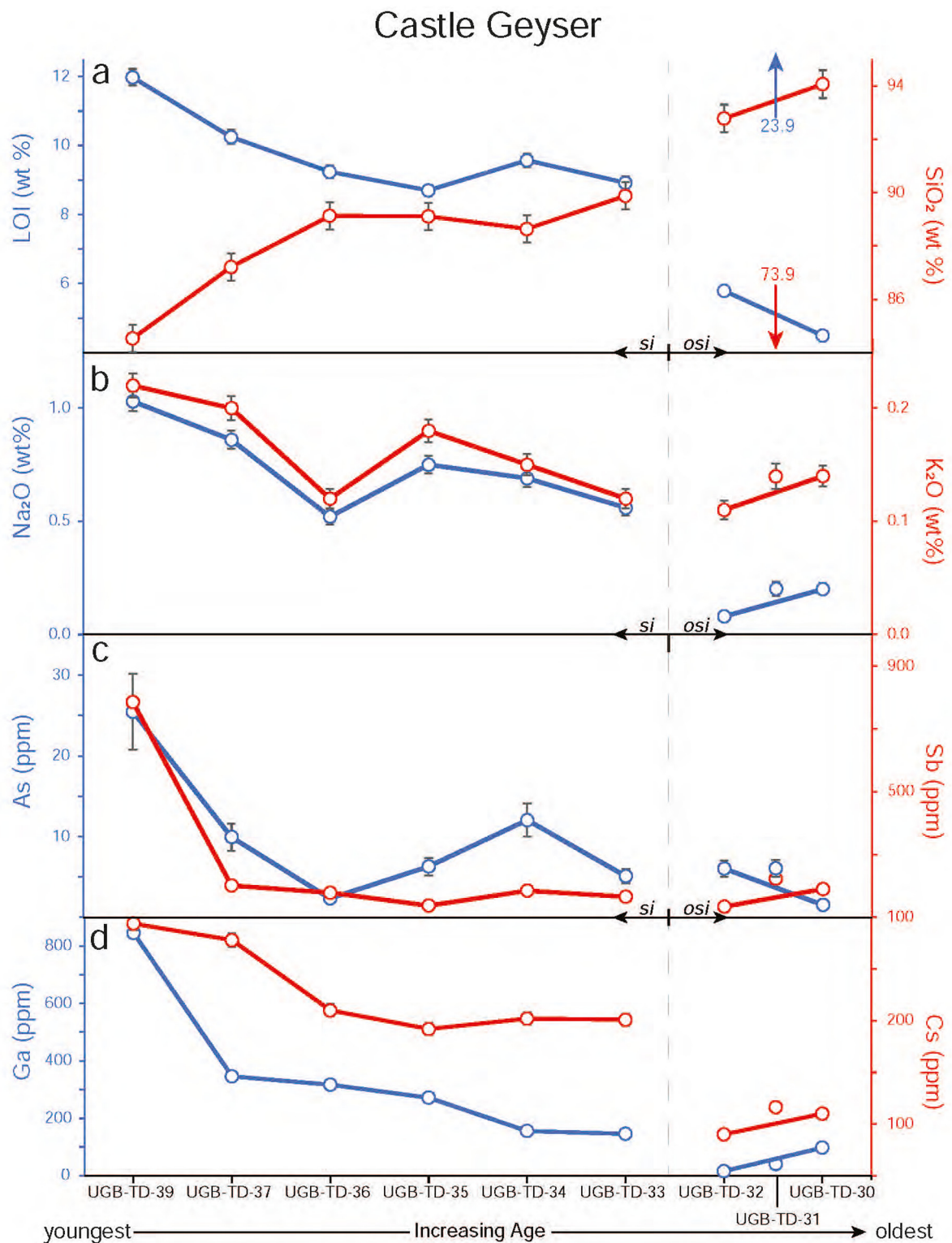
Fig. 10. Concentrations as a function of stratigraphic position at Castle Geyser. The age of samples increases to the right; a break in the lines separates sinter (*si*) and old sinter (*osi*) samples. a) Loss on ignition (LOI; interpreted as water percentage) (blue symbols and curve) and SiO_2 (red symbols and curve). b) Concentration of Na (blue symbols and curve) and K (red symbols and curve). c) Arsenic (As; blue symbols and curve) and antimony (Sb; red symbols and curve) concentrations. d) Gallium (Ga; blue symbols and curve) and cesium (Cs; red symbols and curve) concentrations. Data are tabulated in Churchill et al. (2021). Blue symbols and curves relate to the left Y-axes and red symbols and curves relate to the right Y-axes. Error bars are shown with 2-sigma (95%) confidence. If error bars are not visible it is because they are smaller than the symbols. Major and trace element concentrations in sample UGB-TD-31 are anomalous because of high organic material content. (For interpretation of the references to colour in this figure legend, the reader is referred to the web version of this article.)
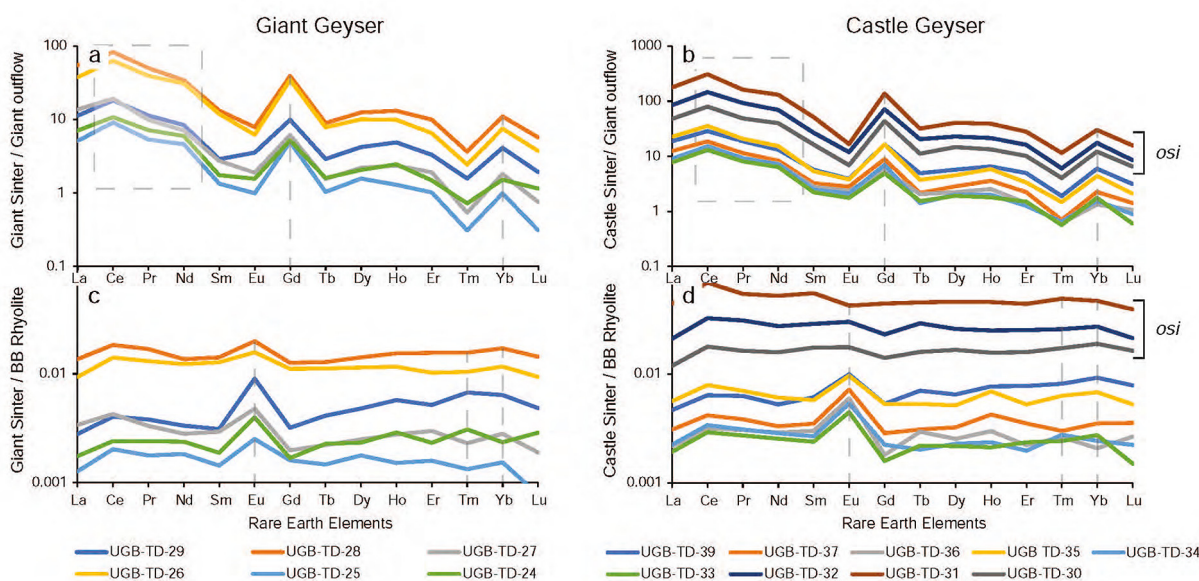
Fig. 11. Rare earth elements (REE) in select sinter samples from Giant and Castle Geysers (data in Churchill et al., 2021). The REE concentrations in the sinter from Giant Geyser are normalized (Y-axes are in logarithmic scale) to a) concentrations in the Giant Geyser thermal water outflow (data from McClesky et al., 2014) and c) concentrations in the Biscuit Basin rhyolite flow (data from Lewis et al., 1997). The REE concentrations in the sinter from Castle Geyser are normalized to b) REE concentrations in the Giant Geyser thermal water outflow (data from McClesky et al., 2014) and d) concentrations in the Biscuit Basin rhyolite flow. The label *osi* is for samples collected from the old sinter unit (Muffler et al., 1982) forming the shield of Castle Geyser. REE anomalies are identified with vertical gray dashed lines. Error bars with 2-sigma (95%) confidence are not visible at this scale.

concentrations in the fluid and in the sinter to SiO_2 concentrations of the sample.

For the sinter, we use K, Na, Si, Cs, Ga and Al concentrations from XRF analysis and Ge, Rb, Sb and As concentrations from LA-ICP-MS analysis (Churchill et al., 2021). For thermal waters, we use average element concentrations from 25 samples collected in the UGB (McCleskey et al., 2014; Hurwitz et al., 2016) (Supplementary material – S1). Because Ge concentration data from thermal waters in the UGB were not available, we used Ge concentrations in a hot spring (Black Pool) in West Thumb Geyser Basin (Gemery-Hill et al., 2007). The chemical composition of Black Pool is similar to the composition of waters from the UGB. For all element pairs, we determined K_D between the youngest samples from Castle Geyser (UGB-TD-39) and Giant Geyser (UGB-TD-29) and thermal water.

Apart from Ge/Si, the calculated K_D values are greater than one, implying that the element with the larger radius is preferentially incorporated in the sinter (Table 2). The calculated K_D values for Ge/Si (0.012–0.015) significantly differ from those determined based on laboratory experiments at 25 °C (K_D = 12.8; Fernandez et al., 2021) but are similar to observations from Iceland where Ge/Si ratios in sinter are much lower than in their associated thermal waters (Arnórsson, 1984). The difference is significant because Ge/Si is often used as a tracer of silica dynamics in hydrothermal systems (Arnórsson, 1984; Evans and Derry, 2002). The difference between the low K_D for the Giant and Castle Geyser samples and the high K_D from the laboratory experiments could be either the result of adsorption and coprecipitation of Ge onto iron hydroxides, or more likely because of temperature-dependent differences in the solubilities of aqueous Ge $(OH)_4$ and $Si(OH)_4$ (Pokrovsky et al., 2006).

There are large uncertainties associated with the K_D values for Ga/Al that are mainly a result of the wide range in the Al (0.30 ± 0.12 mg·l^{-1}) and Ga (17.8 ± 9.48 μg·l^{-1}) concentrations in the thermal water samples. Such variability in thermal water is common, and methods were developed to correct for Al concentrations in multireaction equilibrium geothermometry calculations (Pang and Reed, 1998; King et al., 2016). Despite the large uncertainties, the K_D for Ga/Al is positive for both UGB-TD-29 and UGB-TD-39 (Table 2), suggesting preferential incorporation of Ga into the opal relative to Al. High Ga concentrations were also measured in geyser eggs (a smooth, oval, siliceous pebble found in alkali chloride hot pools) from Old Faithful Geyser (Smith et al., 2018). In some active hydrothermal areas of the Taupo Volcanic Zone (TVZ) in New Zealand, Ga/Al in thermal water is an order of magnitude higher than in fumarolic gas condensates and it is an order of magnitude higher in silica sinter compared with thermal water (Payne, 2016). Chloride complexes are not expected to play a significant role in the transport of Ga at temperatures below approximately 300 °C. The strongest complexes are with ligands such as hydroxide, fluoride, and sulfate (Wood and Samson, 2006).

Several studies have shown that the concentrations of As and Sb in sinters are relatively high (McKenzie et al., 2001; Phoenix et al., 2005; Sanchez-Yanez et al., 2017). The calculated K_D for Sb/As is significantly high: $22,400 \pm 5500$ and $19,000 \pm 4950$ for UGB-TD-29 and UGB-TD-39, respectively (Table 2). This observation indicates that Sb is highly enriched in the sinter compared with the thermal water. The

Table 2
Partition coefficient between water and sinter (K_D) for element pairs.

		Water[a]	±	Sinter[b]	±	K_D[c]	±
UGB-TD-29 (Giant Geyser)							
K/Na	mmol/mol	28	4	160	16	5.9	1.0
Ge/Si	μmol/mol	150	3	1.7	0.2	0.01	0.00
Ga/Al	mmol/mol	31	25	190	40	6.2	5.3
Sb/As	mmol/mol	39	15	22,400	5500	580	270
Cs/Rb	mol/mol	1.3	0.2	3.7	0.1	2.7	0.34
UGB-TD-39 (Castle Geyser)							
K/Na	mmol/mol	28	4	140	9	5.0	0.7
Ge/Si	μmol/mol	150	3	2.2	0.3	0.02	0.00
Ga/Al	mmol/mol	31	25	97	11	3.1	2.6
Sb/As	mmol/mol	39	15	19,000	4950	490	230
Cs/Rb	mol/mol	1.3	0.2	4.4	0.1	3.3	0.40

[a] Average ratios in thermal water samples from the Upper Geyser Basin (Supplementary material – S1).
[b] Element concentrations in the sinter and 2σ uncertainties are from Churchill et al. (2021).
[c] Partition coefficient (dimensionless) calculated with Eq. 1.

Table 3
Silica deposition rates in geyser fields.

Location	Method	Duration years	Rate kg·m^{-2}·yr^{-1}	Reference
Castle Geyser	SfM[a]	5500–11000[b]	1.1–2.2[c]	This study
Yellowstone Lower Geyser Basin	Bacterial mats[d]	0.8	2.5–3.2	Hinman and Lindstrom (1996)
Outcrops in Taupo, New Zealand	Thickness and age	829–3120	2.8–8.7[e]	Lynne et al. (2019)
Australia hot pool, New Zealand	Glass slides	2.4	16.6	Lynne et al. (2019)
Waiotapu, New Zealand	Glass slides	1.2	0.4[f]	Handley et al. (2005)
El Tatio, Chile	Glass slides	0.8	2.5	Nicolau et al. (2014)
Hveragerdi and Geysir, Iceland	Glass slides	2.5	1.4	Tobler et al. (2008)
Krafla, Iceland	Glass slides	2.5	19.5	Tobler et al. (2008)

[a] Structure-from-Motion photogrammetry.
[b] Minimum and maximum estimated age of Castle Geyser.
[c] Deposition rates of 470 to 940 kg yr^{-1} divided by an area of 416 m^2.
[d] Dispersed a powdered corundum layer over the bacterial mats as a bed marker.
[e] Reported as mm yr^{-1}; multiplied by an opal density of 2180 kg m^{-3}.
[f] Reported as mg day^{-1} slide^{-1}; converted by multiplying by reported slide area.

concentrations of iron and sulfur in the water seem to have a large control on the incorporation of As and Sb into the sinter; Sb will preferentially precipitate with silica when Fe concentrations are low, and As will not precipitate with silica unless the Fe and sulfur (mainly sulfide) are at some sufficient concentration (McKenzie et al., 2001). At the El Tatio Geyser Field in Northern Chile, the concentration of total As and Sb in thermal springs are the highest reported for a natural surface water with total As and Sb concentrations of ~0.45 and 0.021 mmol L^{-1} (~34 and 2.6 mg/L), respectively in geyser waters, primarily in the reduced (III) redox state in the discharge. The ferric oxyhydroxides are associated with the microbial mats and some mineral precipitates accumulate substantial As (with >10 wt% arsenate in the mats). Whereas the microbial mats represent a significant reservoir of As in this system, Sb is not associated with the mineral ferric oxides or the mats but is substantially enriched in the silica matrix of the geyserite precipitates (Landrum et al., 2009). At El Tatio, As is predominantly sorbed as arsenate on hydrous ferric oxides (63% molar proportion) and on nodular arsenide micro-mineralization (37% molar proportion), similar to the mineral loellingite (FeAs$_2$) (Alsina et al., 2014). It was also proposed that As is probably present in sinter as a discrete amorphous sulfide phase and that relatively low concentrations of As are a result of the low concentration of sulfide ligands (Parker and Nicholson, 1990). The presence of sulfide in thermal waters can also lead to the formation of thiolated anions (sulfur replacement of oxygen in a compound), and thioarsenates are significantly more prominent and ubiquitous compared with thiolated antimony (Planer-Friedrich et al., 2020). Thus, high degrees of thiolation can hinder co-precipitation of As and silica. Biomineralization might also contribute to enrichment of Sb over As in the sinter. In Champagne Pool (TVZ), Sb was found adsorbed to microbial cell walls at typically twice the concentration of S and As (Phoenix et al., 2005).

The Cs/Rb ratio is only slightly higher in the sinter compared with thermal water ($K_D = 1.3 \pm 0.2$ for both samples). In contrast, hydrothermally altered rhyolites in Yellowstone's UGB are significantly enriched in Cs which is selectively concentrated in the zeolite mineral analcime (Keith et al., 1983).

Sinter samples with high concentrations of organic material (UGB-TD-28 and UGB-TD-31) are also enriched in Ga and Fe along with other trace metals (i.e., Ba, Nb, Th, Y, Zr), relative to the other samples. A similar observation was made in geyserite from Tokaanu in the TVZ, where it was found that the highest concentrations of Tl and Hg are associated with the organic fraction (McKenzie et al., 2001). While we did not examine the role of thermophile microbes in the processes that enrich metals and/or metalloids in the sinter, studies have showed that some heavy metals are preferentially incorporated in silica minerals by microbial activity (Urrutia and Beveridge, 1994; Konhauser and Ferris, 1996; Jones et al., 2001; McKenzie et al., 2001; Konhauser et al., 2001; Mountain et al., 2003; Phoenix et al., 2005). Active microbial

mats in recent siliceous sinter deposits from an alkaline hot spring in Yellowstone's Lower Geyser Basin were also found to sequester and preserve Ga, Fe, and possibly Mn (Gangidine et al., 2020).

Rare earth element (REE) concentrations in the sinter were normalized to concentrations in UGB thermal water (Sample 09WA157 in McCleskey et al., 2014) and to the underlying Biscuit Basin rhyolite flow (Lewis et al., 1997). REE concentrations in sinter are 2–3 orders of magnitude higher than in the thermal water, and 2–3 orders of magnitude less than in the rhyolite (Fig. 11). This finding implies that the solubilities of REE concentrations in alkaline-chloride Cl waters are very low, especially when compared to acid-sulfate (low pH) waters (Lewis et al., 1997). When REE concentrations in the sinter are normalized to concentrations in the alkaline-chloride water, LREE in the sinter are enriched compared to the HREE, there are positive Gd and Yb anomalies and a small negative Eu anomaly (Fig. 11a,b). Some sinters from the Tibetan Plateau in China have similar patterns of LREE enrichments, including a positive Gd anomaly (but not Yb anomaly) and a small negative Eu anomaly (Feng et al., 2014). Samples of lithified sinters that underlie the modern sinters at Geysir in Iceland are also relatively enriched in LREE, but with no apparent Gd, Yb, and Eu anomalies (Jones and Renaut, 2021). When REE concentrations in the sinter are normalized to the underlying rhyolite (Biscuit Basin flow), the profiles are mostly flat (no apparent enrichment of individual or group of elements) but with relatively large positive Eu anomalies and much smaller Tm and Yb anomalies (Fig. 11c,d). The Eu anomalies are likely a result of either (1) Eu^{2+} impurities in the SiO_2 lattice or (2) small Eu^{2+}-rich feldspar grains, sourced from Eu^{2+}-rich plagioclase feldspars in the rhyolites (Lewis et al., 1997; Möller, 2000; Feng et al., 2014). Sinter samples with the highest REE concentrations at Giant (UGB-TD-26 and -28) and Castle (UGB-TD-31 and -32) Geysers are also relatively enriched in organic material. This enrichment might suggest that microbes either preferentially sequester REE elements, that these REE metals preferentially adsorb onto organic material, or that organic molecules serve as efficient ligands.

In Paleozoic sinter deposits from the Drummond Basin in Australia it was proposed that fluorine is the ligand that forms REE complexes during hydrothermal activity (Uysal et al., 2011). However, it was demonstrated more recently that REE-fluoride complexes are insignificant in REE transport compared with REE-chloride complexes (Migdisov and Williams-Jones, 2014), which have been shown to be a very effective ligand for metal complexes in high-temperature aqueous solutions (Douville et al., 1999; Mayanovic et al., 2007, 2009; Migdisov et al., 2016). Since thermal water in the UGB has high concentrations of dissolved chloride (typically 350–500 mg·l^{-1}), it is likely that it is a major ligand in the sinter deposits. However, with the data available, we were unable to determine the mechanisms through which REE are incorporated and fractionated in the sinter.

4.4. Major and trace element variation through time

At both geysers, the concentrations of most metals and metalloids decrease with increasing crystallinity, increasing SiO_2 concentrations, and decreasing LOI. For example, the concentrations of Cs, Ga and Sb decrease from 294 ± 3.3, 845 ± 5.5 and 785 ± 2.8 ppm in the youngest sample (UGB-TD-39 with LOI of 12 wt%) to 104 ± 2.5, 98 ± 1.8, and 191 ± 2.9 ppm, respectively, in an older sample (UGB-TD-30 with LOI of 4.5 wt%) from Castle Geyser. The temporal trend at Giant Geyser is similar (Fig. 9d; 10c,d). Oxide concentrations of Al_2O_3, MnO, CaO, and Na_2O decrease by 50% or more from the youngest to the oldest sample at each geyser. Thus, as sinter dehydrates, metals and metalloids either preferentially partition into the exsolved water, are expelled from the more crystalline silica lattice, or a combination of both factors.

In the Puchuldiza geothermal field (northern Chilean Altiplano), analysis of the trends between sinter crystallinity and element concentration found that metalloids (i.e., As and B) are mainly concentrated in the immature silica phases, whereas metals (i.e., Ag and Au) are mostly enriched in the crystalline silica phases (Sanchez-Yanez et al., 2017). Using magic angle spinning nuclear magnetic resonance (MAS NMR) it was shown that in geyserite of the Targejia hot spring deposit in Tibet, Cs is coordinated by O^{2-}, OH^{-}, and H_2O as a network modifying cation. As Cs-bearing geyserite ages and dehydrates, Cs concentration decreases as it is leached out from the opals as it loses its original coordination environment in the silicate framework (Zhou et al., 2013). Compared with concentrations measured in sinter from this study, metal and metalloid concentrations from the ~9.5 Ma Atastra Creek sinter in eastern California are similar or greater (Sb = 393 ppm, As = 532 ppm; Campbell et al., 2018). Similarly, studies of Paleozoic sinters (Sillitoe, 2015; Pirajno, 2020; Cunneen and Sillitoe, 1989; White et al., 1989) have reported greater enrichment for some metals (Ba and Sr; Uysal et al., 2011) than in the Holocene sinter from this study.

4.5. Future work

We propose several research directions that are not widely used in the study of silica sinter deposits and can build upon the results of this study to improve the understanding of some processes discussed in this paper. To better quantify geyser construction, erosion and deposition rates, and quantify mineral transformation and dehydration rates, new methods for dating sinter deposits are needed to overcome the challenges with radiometric dating (Churchill et al., 2020).

Our study provides new information and an improved understanding on the partitioning of elements between sinter and the thermal water from which they are deposited. The data also demonstrate that there are large chemical variations in the sinter as it matures. However, to better understand and quantify how various metals and metalloids are incorporated into the sinter, further insight into what ligands form the metal complexes and how they associate with water is needed. High-resolution imaging with SEM and transmitted electron microscopy (TEM) can better help characterize microbial–silica interactions (Konhauser and Ferris, 1996; Konhauser et al., 2001; Gangidine et al., 2020).

Micro-proton-induced X-ray Emission (micro-PIXE) is an accurate analytical method that makes it possible to achieve trace element detection limits at the ppm level in silicate minerals and glasses and to map the internal distribution within small samples (Heirwegh et al., 2016). For sinter samples, Micro-PIXE could allow for the identification of the ligands that form metal complexes. We also suggest that better determination of the components measured as LOI could provide more accurate information on dehydration (or devolatilization), and on the ligands that form metal complexes. For example, the elevated LOI for sample UGB-TD-31 (24 wt%) was determined to be a result of abundant organic material and it also has the highest REE concentration out of all the samples. Combining electron microprobe and micro–Fourier transform infrared (FTIR) analyses was shown to provide information on the distribution of different types of water (molecular water and silanols) in opal as it dehydrates (Day and Jones, 2008).

Finally, there is an opportunity to use stable isotopes of $\delta^{10}Li$ (Cullen et al., 2021), $\delta^{30}Si$ (Chen et al., 2020), $\delta^{74}Ge$ (Rouxel and Luais, 2017), $\delta^{71}Ga$ (Payne, 2016), and $\delta^{123}Sb$ (Zhai et al., 2021) to quantify isotopic fractionation of these elements, which typically have elevated concentrations in hydrothermal systems, both when deposited with silica from the thermal water and as the sinter matures.

5. Conclusions

The purpose of this study was to characterize the size and structure of two large geyser cones, how elements are incorporated into sinter relative to the thermal waters they are deposited from, and the time-dependence of dehydration, silica mineral diagenesis, and chemical variations in the sinter. Based on the three-dimensional models of Giant and Castle Geysers in Yellowstone National Park's Upper Geyser Basin, and on the analyses of samples collected along the stratigraphic column of these geysers, we conclude:

1. The approximate masses of sinter in Giant and Castle Geysers are ~2 kton and ~5 kton, respectively. The minimum and maximum silica precipitation rates at Castle Geyser are 470–940 kg·yr^{-1} based on an inferred maximum and minimum ages of 11 ka and 5.5 ka and assuming continuous deposition. These calculated rates have large uncertainties because they do not account for erosion, climate variations that control deposition rates through water discharge, air temperature and evaporation. The calculated deposition rates are within the same order of magnitude as those determined with other methods and over shorter durations for other silica sinter deposits in the world.

2. Based on measured water discharge rates and silica concentrations at Lone Star Geyser, a large cone geyser with approximately the same structure and volume as Giant and Castle Geysers, we estimate that the maximum long-term silica deposition rate is ~2% of the total mass of silica discharge from Castle Geyser.

3. Sinter deposits from Giant Geyser consist of opal-A/C and opal-A microspheres and have lower structural order and higher concentrations of water compared to the older samples. Samples from the base of Giant Geyser contain significant amounts of quartz. Sinter deposits from Castle Geyser are composed of immature botryoidal, coalesced microspheres of opal-A with low structural order (FWHM ~6.3 2θ) and high amounts of water (>8.9 wt%). However, crystalline opal might be present in the internal and inaccessible parts of the geyser cone. The older sinter deposits from the shield of Castle Geyser contain more mature SiO_2 polymorphs (opal-A/C, opal-CT and quartz), contain less water (<5.8 wt%), and exhibit higher structural order (FWHM <5.5° 2θ).

4. The concentrations of SiO_2 (>84.5 wt%), other major oxides with concentrations of 0.1–0.4 wt% (Na_2O, K_2O and Al_2O_3), trace elements with concentrations of >100 ppm (Ga, Cs, Sb) and trace elements with concentrations of 1–100 ppm (As, Ba, Cr, Cu, Ge, Ni, Pb, Rb, Sr, V, Zn, Zr) in the sinter deposits of Giant and Castle Geysers are mostly similar to those in siliceous sinter deposited in other hydrothermal areas.

5. Concentrations of most metals and metalloids, such as As, Ga, Cs, Sb and Rb, in the sinter from Giant and Castle Geysers decrease with increasing relative age.

6. We calculated partition coefficients (K_D) for pairs of element ratios in the sinter over the same ratio in the thermal water, where values greater than one imply higher ratios in the sinter compared with ratios in the thermal water. In Castle and Giant Geysers, respectively, the K_D for K/Na (5.0 ± 0.7 and 5.9 ± 1.0), Cs/Rb (3.3 ± 0.40 and 2.7 ± 0.34), Ga/Al (3.1 ± 2.6 and 6.2 ± 5.3) and Sb/As (492 ± 230 and 580 ± 267) imply a higher ratio in the

sinter, whereas the K_D for Ge/Si (0.02 ± 0.00 and 0.01 ± 0.00) implies a higher ratio in the thermal water.

7. Rare earth element (REE) concentrations in the sinter are 2–3 orders of magnitude higher than in the alkaline-chloride thermal water from which the sinter is deposited. REE concentrations in the sinter normalized to concentrations in the water indicate that light REE in the sinter are enriched compared to the heavy REE, there are positive Gd and Yb anomalies and a small negative Eu anomaly.

8. Sinter samples enriched in organic material contain the highest REE, Ga and Fe concentrations, likely suggesting either uptake by microbes, or that organic molecules act as ligands forming metal complexes.

Declaration of Competing Interest

Acknowledgments

Appendix A. Supplementary data

Supplementary data to this article can be found online at https://doi.org/10.1016/j.jvolgeores.2021.107391.

References

Abedini, A.A., Robinson, J.E., Muffler, L.J.P., White, D.E., Beeson, M.H., Truesdell, A.H., 2015. Database for the Geologic Map of Upper Geyser Basin, Yellowstone National Park. Geological Survey Data Series, Wyoming. U.S https://doi.org/10.3133/ds911 911, scale 1:4,800.

Alsina, M.A., Zanella, L., Hoel, C., Pizarro, G.E., Gaillard, J.F., Pasten, P.A., 2014. Arsenic speciation in sinter mineralization from a hydrothermal channel of El Tatio geothermal field, Chile. J. Hydrol. 518, 434–446. https://doi.org/10.1016/j.jhydrol.2013.04.012.

Arnórsson, S., 1984. Germanium in Icelandic geothermal systems. Geochim. Cosmochim. Acta 48, 2489–2502. https://doi.org/10.1016/0016-7037(84)90300-4.

Ballantyne, J.M., Moore, J.N., 1988. Arsenic geochemistry in geothermal systems. Geochim. Cosmochim. Acta 52, 475–483. https://doi.org/10.1016/0016-7037(88)90102-0.

Bowell, R.J., Alpers, C.N., Jamieson, H.E., Nordstrom, D.K., Majzlan, J., 2014. The environmental geochemistry of arsenic—an overview. Rev. Mineral. Geochem. 79, 1–16. https://doi.org/10.2138/rmg.2014.79.1.

Braunstein, D., Lowe, D.R., 2001. Relationship between spring and geyser activity and the deposition and morphology of high temperature ($> 73°C$) siliceous sinter, Yellowstone National Park, Wyoming, USA. J. Sediment. Res. 71, 747–763. https://doi.org/10.1306/2DC40965-0E47-11D7-8643000102C1865D.

Brown, K.L., Simmons, S.F., 2003. Precious metals in high-temperature geothermal systems in New Zealand. Geothermics 32, 619–625. https://doi.org/10.1016/S0375-6505(03)00049-X.

Bryan, T.S., 2018. The Geysers of Yellowstone. 5th ed. University Press of Colorado, Boulder.

Cady, S.L., Skok, J.R., Gulick, V.G., Berger, J.A., Hinman, N.W., 2018. Siliceous Hot Spring Deposits: Why They Remain Key Astrobiological Targets. From Habitability to Life on Mars. , pp. 179–210 https://doi.org/10.1016/B978-0-12-809935-3.00007-4.

Campbell, K.A., Guido, D.M., Gautret, P., Foucher, F., Ramboz, C., Westall, F., 2015. Geyserite in hot-spring siliceous sinter: Window on Earth's hottest terrestrial (paleo) environment and its extreme life. Earth Sci. Rev. 148, 44–64. https://doi.org/10.1016/j.earscirev.2015.05.009.

Campbell, K.A., Guido, D.M., John, D.A., Vikre, P.G., Rhys, D., Hamilton, A., 2018. The Miocene Atastra Creek sinter (Bodie Hills volcanic field, California and Nevada): 4D evolution of a geomorphically intact siliceous hot spring deposit. J. Volcanol. Geotherm. Res. 370, 65–81. https://doi.org/10.1016/j.jvolgeores.2018.12.006.

Chen, X.Y., Chafetz, H.S., Lapen, T.J., 2020. Silicon isotope variations in hydrothermal systems at Yellowstone National Park, Wyoming, USA. Geochim. Cosmochim. Acta 283, 184–200. https://doi.org/10.1016/j.gca.2020.06.004.

Christiansen, R.L., 2001. The Quaternary and Pliocene Yellowstone Plateau volcanic field of Wyoming, Idaho, and Montana. U.S. Geological Survey Professional Paper 729-G. https://doi.org/10.3133/pp729G.

Churchill, D.M., Manga, M., Hurwitz, S., Peek, S., Licciardi, J.M., Paces, J.B., 2020. Dating silica sinter (geyserite): a cautionary tale. J. Volcanol. Geotherm. Res. 402. https://doi.org/10.1016/j.jvolgeores.2020.106991.

Churchill, D.M., Peek, S., Hurwitz, S., Manga, M., Damby, D.E., Conrey, R., Paces, J.B., Licciardi, J.M., 2021. Mineralogy, chemistry and isotope composition of silica sinter deposits from the Upper Geyser Basin, Yellowstone National Park (ver. 2.0, April 2021). U.S. Geological Survey https://doi.org/10.5066/P90SU3TV.

Clark, J.R., Williams-Jones, A.E., 1990. Analogues of epithermal gold–silver deposition in geothermal well scales. Nature 346, 644–645. https://doi.org/10.1038/346644a0.

Cullen, J.T., Hurwitz, S., Barnes, J.D., Lassiter, J.C., Penniston-Dorland, S., Kasemann, S.A., Thordsen, J.J., 2019. Temperature-dependent variations in mineralogy, major element chemistry and the stable isotopes of boron, lithium and chlorine resulting from hydration of rhyolite: Constraints from hydrothermal experiments at 150 to 350° C and 25 MPa. Geochim. Cosmochim. Acta 261, 269–287. https://doi.org/10.1016/j.gca.2019.07.012.

Cullen, J.T., Hurwitz, S., Barnes, J.D., Lassiter, J.C., Penniston-Dorland, S., Meixner, A., Wilckens, F., Kasemann, S.A., McCleskey, R.B., 2021. The Systematics of Chlorine, Lithium and Boron and $\delta 37Cl$, $\delta 7Li$ and $\delta 11B$ in the Hydrothermal System of the Yellowstone Plateau Volcanic Field. Geochem. Geophys. Geosyst. https://doi.org/10.1029/2020GC009589.

Cunneen, R., Sillitoe, R.H., 1989. Paleozoic hot spring sinter in the Drummond Basin, Queensland, Australia. Econ. Geol. 84, 135–142. https://doi.org/10.2113/gsecongeo.84.1.135.

Day, R., Jones, B., 2008. Variations in water content in opal-A and opal-CT from geyser discharge aprons. J. Sediment. Res. 78, 301–315. https://doi.org/10.2110/jsr.2008.030.

Djokic, T., Van Kranendonk, M.J., Campbell, K.A., Walter, M.R., Ward, C.R., 2017. Earliest signs of life on land preserved in ca. 3.5 Ga hot spring deposits. Nat. Commun. 8, 1–9. https://doi.org/10.1038/ncomms15263.

Douville, E., Bienvenu, P., Charlou, J.L., Donval, J.P., Fouquet, Y., Appriou, P., Gamo, T., 1999. Yttrium and rare earth elements in fluids from various hydrothermal systems. Geochim. Cosmochim. Acta 63, 627–643. https://doi.org/10.1016/S0016-7037(99)00024-1.

Ellis, A.J., Sewell, J.R., 1963. Boron in waters and rocks of New Zealand hydrothermal areas. N. Z. J. Sci. 6, 589–606.

Evans, M.J., Derry, L.A., 2002. Quartz control of high germanium/silicon ratios in geothermal waters. Geology 30 (11), 1019. https://doi.org/10.1130/0091-7613(2002)030<1019:qcohgs>2.0.co;2.

Feng, J.-L., Zhao, Z.-H., Chen, F., Hu, H.-P., 2014. Rare earth elements in sinters from the geothermal waters (hot springs) on the Tibetan Plateau, China. J. Volcanol. Geotherm. Res. 287, 1–11. https://doi.org/10.1016/j.jvolgeores.2014.09.009.

Fernandez, N.M., Perez-Fodich, A., Derry, L.A., Druhan, J.L., 2021. A first look at Ge/Si partitioning during amorphous silica precipitation: Implications for Ge/Si as a tracer of fluid-silicate interactions. Geochim. Cosmochim. Acta 297, 158–178. https://doi.org/10.1016/j.gca.2021.01.007.

Filella, M., Williams, P.A., Belzile, N., 2009. Antimony in the environment: knowns and unknowns. Environ. Chem. 6, 95–105. https://doi.org/10.1071/EN09007.

Foley, D., 2006. Dating Castle Geyser: preliminary results and broad speculations on the geologic development of geysers and hydrothermal systems in Yellowstone National Park, Wyoming, USA. Trans. - Geotherm. Resour. Counc. 30, 413–417.. https://publications.mygeoenergynow.org/grc/1025067.pdf.

Foley, D., Fournier, R.O., Heasler, H.P., Hinckley, B., Ingebritsen, S.E., Lowenstern, J.B., Susong, D.D., 2014. Hydrogeology of the ald faithful area, Yellowstone National Park, Wyoming, and its relevance to natural resources and infrastructure. (No. 2014-1058). U.S. Geological Survey, p. 28 https://doi.org/10.3133/ofr20141058.

Fournier, R.O., 1989. Geochemistry and dynamics of the Yellowstone National Park hydrothermal system. Annu. Rev. Earth Planet. Sci. 17, 13–53. https://doi.org/10.1146/annurev.ea.17.050189.000305.

Fournier, R.O., Kennedy, B.M., Aoki, M., Thompson, J.M., 1994. Correlation of gold in siliceous sinters with $^3He/^4He$ in hot spring waters of Yellowstone National Park. Geochim. Cosmochim. Acta 58, 5401–5419. https://doi.org/10.1016/0016-7037(94)90238-0.

Gangidine, A., Havig, J.R., Fike, D.A., Jones, C., Hamilton, T.L., Czaja, A.D., 2020. Trace element concentrations in hydrothermal silica deposits as a potential biosignature. Astrobiology 20, 525–536. https://doi.org/10.1089/ast.2018.1994.

Gemery-Hill, P.A., Shanks III, W.C., Balistrieri, L.S., Lee, G.K., 2007. Geochemical data for selected rivers, lake waters, hydrothermal vents, and subaerial geysers in Yellowstone National Park, Wyoming and vicinity, 1996–2004. In: Morgan, L.A. (Ed.), Integrated Geoscience Studies in the Greater Yellowstone Area: Volcanic, Hydrothermal and Tectonic Processes in the Yellowstone Geoecosystem. 1717. U.S. Geological Survey Professional Paper , pp. 365–426.. https://pubs.usgs.gov/pp/1717/downloads/pdf/p1717L.pdf.

Graedel, T.E., Harper, E.M., Nassar, N.T., Nuss, P., Reck, B.K., 2015. Criticality of metals and metalloids. Proc. Natl. Acad. Sci. 112, 4257–4262. https://doi.org/10.1073/pnas.1500415112.

Guidry, S.A., Chafetz, H.S., 2003. Anatomy of siliceous hot springs: examples from Yellowstone National Park, Wyoming, USA. Sediment. Geol. 157, 71–106. https://doi.org/10.1016/S0037-0738(02)00195-1.

Hamilton, A., Campbell, K., Rowland, J., Browne, P., 2017. The Kohuamuri siliceous sinter as a vector for epithermal mineralisation, Coromandel Volcanic Zone, New Zealand. Mineral. Deposita 52, 181–196. https://doi.org/10.1007/s00126-016-0658-8.

Handley, K.M., Campbell, K.A., Mountain, B.W., Browne, P.R.L, 2005. Abiotic–biotic controls on the origin and development of spicular sinter: in situ growth experiments, Champagne Pool, Waiotapu, New Zealand. Geobiology 3, 93–114. https://doi.org/10.1111/j.1472-4669.2005.00046.x.

Hayden, F.V., 1883. Twelfth Annual Report of the United States Geological and Geographical Survey of the Territories: A Report of Progress of the Exploration in Wyoming and Idaho for the Year 1878, Part II. Yellowstone National Park. United States. Dept. of the Interior. Washington D.C. Government Printing Office https://doi.org/10.3133/70038941.

Heasler, H.P., Jaworowski, C., Foley, D., 2009. Geothermal systems and monitoring hydrothermal features. Geological Monitoring. Special Paper of the Geological Society of America, pp. 105–140 https://doi.org/10.1130/2009.monitoring(05).

Heirwegh, C.M., Campbell, J.L., Czamanske, G.K., 2016. Refinement of major-and minor-element PIXE analysis of rocks and minerals. Nucl. Instrum. Methods Phys. Res., Sect. B 366, 40–50. https://doi.org/10.1016/j.nimb.2015.10.018.

Herdianita, N.R., Browne, P.R.L., Rodgers, K.A., Campbell, K.A., 2000. Mineralogical and textural changes accompanying ageing of silica sinter. Mineral. Deposita 35, 48–62. https://doi.org/10.1007/s001260050005.

Hinman, N.W., Kotler, J., 2013. Aluminum in silica phases formed in hot springs. Procedia Earth Planet. Sci. 7, 365–368. https://doi.org/10.1016/j.proeps.2013.03.078.

Hinman, N.W., Lindstrom, R.F., 1996. Seasonal changes in silica deposition in hot spring systems. Chem. Geol. 132, 237–246. https://doi.org/10.1016/S0009-2541(96)00060-5.

Hinman, N.W., Walter, M.R., 2005. Textural preservation in siliceous hot spring deposits during early diagenesis: examples from Yellowstone National Park and Nevada, USA. J. Sediment. Res. 75, 200–215. https://doi.org/10.2110/jsr.2005.016.

Hurwitz, S., Lowenstern, J.B., 2014. Dynamics of the Yellowstone hydrothermal system. Rev. Geophys. 52, 375–411. https://doi.org/10.1002/2014RG000452.

Hurwitz, S., Manga, M., 2017. The Fascinating and Complex Dynamics of Geyser Eruptions. Annu. Rev. Earth Planet. Sci. 45, 31–59. https://doi.org/10.1146/annurev-earth-063016-015605.

Hurwitz, S., Hunt, A.G., Evans, W.C., 2012. Temporal variations of geyser water chemistry in the Upper Geyser Basin, Yellowstone National Park, USA. Geochem. Geophys. Geosyst. 13. https://doi.org/10.1029/2012gc004388.

Hurwitz, S., Clor, L.E., McCleskey, R.B., Nordstrom, D.K., Hunt, A.G., Evans, W.C., 2016. Dissolved gases in hydrothermal (phreatic) and geyser eruptions at Yellowstone National Park, USA. Geology 44, 235–238. https://doi.org/10.1130/G37478.1.

Hurwitz, S., King, J.C., Pederson, G.T., Martin, J.T., Damby, D.E., Manga, M., Hungerford, J.D., Peek, S., 2020. Yellowstone's old faithful Geyser shut down by a severe thirteenth century drought. Geophys. Res. Lett. 47. https://doi.org/10.1029/2020GL089871 p. e2020GL089871.

Hurwitz, S., Manga, M., Campbell, K.A., Muñoz-Saez, C., Eibl, E.P.S., 2021. Why study geysers? Eos 102. https://doi.org/10.1029/2021EO161365.

Ichikuni, M., 1968. Uptake of boron by siliceous sinters. Geochem. J. 2, 105–109.. http://www.terrapub.co.jp/journals/GJ/pdf/0202/02020105.pdf.

Ichikuni, M., 1970. Incorporation of Siliceous and Iron into Siliceous Sinters. Chem. Geol. 6, 273–279. https://doi.org/10.1016/0009-2541(70)90028-8.

Johnson, D.B., Hooper, P., Conrey, R., 1999. XRF analysis of rocks and minerals for major and trace elements on a single low dilution Li-tetraborate fused bead. Adv. X-ray Anal. 41, 843–867.

Jones, B., 2020. Siliceous sinters in thermal spring systems: review of their mineralogy, diagenesis, and fabrics. Sediment. Geol. 416, 105820. https://doi.org/10.1016/j.sedgeo.2020.105820.

Jones, B., Renaut, R.W., 2003. Hot spring and geyser sinters: the integrated product of precipitation, replacement, and deposition. Can. J. Earth Sci. 40, 1549–1569. https://doi.org/10.1139/e03-078.

Jones, B., Renaut, R.W., 2004. Water content of opal-a: implications for the origin of laminae in geyserite and sinter. J. Sediment. Res. 74, 117–128. https://doi.org/10.1306/052403740117.

Jones, B., Renaut, R.W., 2021. Multifaceted incremental growth of a geyser discharge apron–evidence from Geysir, Haukadalur, Iceland. Sediment. Geol. 419, 105905. https://doi.org/10.1016/j.sedgeo.2021.105905.

Jones, B., Renaut, R.W., Rosen, M.R., 2001. Biogenicity of gold- and silver-bearing siliceous sinters forming in hot (75°C) anaerobic spring-waters of Champagne Pool, Waiotapu, North Island, New Zealand. J. Geol. Soc. 158, 895–911. https://doi.org/10.1144/0016-764900-131.

Kaasalainen, H., Stefánsson, A., 2012. The chemistry of trace elements in surface geothermal waters and steam, Iceland. Chem. Geol. 330, 60–85. https://doi.org/10.1016/j.chemgeo.2012.08.019.

Karlstrom, L., Hurwitz, S., Sohn, R., Vandemeulebrouck, J., Murphy, F., Rudolph, M.L., Johnston, M.J., Manga, M., McCleskey, R.B., 2013. Eruptions at lone star geyser, Yellowstone National Park, USA: 1. Energetics and eruption dynamics. J. Geophys. Res. 118, 4048–4062. https://doi.org/10.1002/jgrb.50251.

Keith, T.E., Thompson, J.M., Mays, R.E., 1983. Selective concentration of cesium in analcime during hydrothermal alteration, Yellowstone National Park, Wyoming. Geochim. Cosmochim. Acta 47, 795–804. https://doi.org/10.1016/0016-7037(83)90113-8.

King, J.M., Hurwitz, S., Lowenstern, J.B., Nordstrom, D.K., McCleskey, R.B., 2016. Multireaction equilibrium geothermometry: a sensitivity analysis using data from the lower Geyser Basin, Yellowstone National Park, USA. J. Volcanol. Geotherm. Res. 328, 105–114. https://doi.org/10.1016/j.jvolgeores.2016.10.010.

Konhauser, K.O., Ferris, F.G., 1996. Diversity of iron and silica precipitation by microbial mats in hydrothermal waters, Iceland: implications for Precambrian iron formations. Geology 24, 323–326. https://doi.org/10.1130/0091-7613(1996)024<0323:DOIASP>2.3.CO;2.

Konhauser, K.O., Phoenix, R., Bottrell, S.H., Adams, D.G., Head, I.M., 2001. Microbial-silica interactions in Icelandic hot spring sinter: possible analogues for some Precambrian siliceous stromatolites. Sedimentology 48, 415–433. https://doi.org/10.1046/j.1365-3091.2001.00372.x.

Landrum, J.T., Bennett, P.C., Engel, A.S., Alsina, M.A., Pastén, P.A., Milliken, K., 2009. Partitioning geochemistry of arsenic and antimony, El Tatio geyser field, Chile. Appl. Geochem. 24, 664–676. https://doi.org/10.1016/j.apgeochem.2008.12.024.

Lewis, A.J., Palmer, M.R., Sturchio, N.C., Kemp, A.J., 1997. The rare earth element geochemistry of acid-sulphate and acid-sulphate-chloride geothermal systems from Yellowstone National Park, USA. Geochim. Cosmochim. Acta 61, 695–706. https://doi.org/10.1016/S0016-7037(96)00384-5.

Licciardi, J.M., Pierce, K.L., 2018. History and dynamics of the Greater Yellowstone Glacial System during the last two glaciations. Quat. Sci. Rev. 200, 1–33. https://doi.org/10.1016/j.quascirev.2018.08.027.

Liesegang, M., Tomaschek, F., 2020. Tracing the continental diagenetic loop of the opal-A to opal-CT transformation with X-ray diffraction. Sediment. Geol. 398, 105603. https://doi.org/10.1016/j.sedgeo.2020.105603.

Lowe, D.R., Braunstein, D., 2003. Microstructure of high-temperature (>73 C) siliceous sinter deposited around hot springs and geysers, Yellowstone National Park: the role of biological and abiological processes in sedimentation. Can. J. Earth Sci. 40, 1611–1642. https://doi.org/10.1139/e03-066.

Lowenstern, J.B., Hurwitz, S., McGeehin, J.P., 2016. Radiocarbon dating of silica sinter deposits in shallow drill cores from the Upper Geyser Basin, Yellowstone National Park. J. Volcanol. Geotherm. Res. 310, 132–136. https://doi.org/10.1016/j.jvolgeores.2015.12.005.

Lynne, B.Y., 2012. Mapping vent to distal-apron hot spring paleo-flow pathways using siliceous sinter architecture. Geothermics 43, 3–24. https://doi.org/10.1016/j.geothermics.2012.01.004.

Lynne, B.Y., Campbell, K.A., 2004. Morphologic and mineralogic transitions from opal-A to opal-CT in low-temperature siliceous sinter diagenesis, Taupo Volcanic Zone, New Zealand. J. Sediment. Res. 74, 561–579. https://doi.org/10.1306/011704740561.

Lynne, B.Y., Campbell, K.A., James, B.J., Browne, P.R., Moore, J., 2007. Tracking Crystallinity in Siliceous hot-spring deposits. Am. J. Sci. 307, 612–641. https://doi.org/10.2475/03.2007.03.

Lynne, B.Y., Heasler, H., Jaworowski, C., Foley, D., Smith, I.J., Smith, G.J., Sahdarani, D., 2017. Using ground penetrating radar, scanning electron microscopy and thermal infrared imagery to document near-surface hydrological changes in the old faithful Geyser area, Yellowstone National Park, U.S.A. Geothermics 68, 33–53. https://doi.org/10.1016/j.geothermics.2017.02.007.

Lynne, B.Y., Boudreau, A., Smith, I.J., Smith, G.J., 2019. Silica accumulation rates for siliceous sinter at Orakei Korako geothermal field, Taupo Volcanic Zone, New Zealand. Geothermics 78, 50–61. https://doi.org/10.1016/j.geothermics.2018.11.007.

Månberger, A., Johansson, B., 2019. The geopolitics of metals and metalloids used for the renewable energy transition. Energy Strategy Rev. 26, 100394. https://doi.org/10.1016/j.esr.2019.100394.

Matthews, N.A., 2008. Aerial and Close-Range Photogrammetric Technology: Providing Resource Documentation, Interpretation, and Preservation. Technical Note 428. U.S. Department of the Interior, Bureau of Land Management, National Operations Center, Denver, Colorado 42 pp https://www.blm.gov/sites/blm.gov/files/documents/files/Library_BLMTechnicalNote428_0.pdf.

Matthews, N.E., Vazquez, J.A., Calvert, A.T., 2015. Age of the Lava Creek supereruption and magma chamber assembly at Yellowstone based on $^{40}Ar/^{39}Ar$ and U-P b dating of sanidine and zircon crystals. Geochem. Geophys. Geosyst. 16, 2508–2528. https://doi.org/10.1002/2015GC005881.

Mayanovic, R.A., Anderson, A.J., Bassett, W.A., Chou, I.-M., 2007. On the formation and structure of rare-earth element complexes in aqueous solutions under hydrothermal conditions with new data on gadolinium aqua and chloro complexes. Chem. Geol. 239, 266–283. https://doi.org/10.1016/j.chemgeo.2006.10.004.

Mayanovic, R.A., Anderson, A.J., Bassett, W.A., Chou, I.-M., 2009. The structure and stability of aqueous rare-earth elements in hydrothermal fluids: New results on neodymium (III) aqua and chloroaqua complexes in aqueous solutions to 500 °C and 520 MPa. Chem. Geol. 259, 30–38. https://doi.org/10.1016/j.chemgeo.2008.08.011.

McCleskey, R.B., Chiu, R.B., Nordstrom, D.K., Campbell, K.M., Roth, D.A., Ball, J.W., Plowman, T.I., 2014. Water-Chemistry Data for Selected Springs, Geysers, and Streams in Yellowstone National Park, Wyoming, Beginning., p. 2009 https://doi.org/10.5066/F7M043FS.

McKenzie, E.J., Brown, K.L., Cady, S.L., Campbell, K.A., 2001. Trace metal chemistry and silicification of microorganisms in geothermal sinter, Taupo Volcanic Zone, New Zealand. Geothermics 30, 483–502. https://doi.org/10.1016/S0375-6505(01)00004-9.

Migdisov, A.A., Williams-Jones, A.E., 2014. Hydrothermal transport and deposition of the rare earth elements by fluorine-bearing aqueous liquids. Mineral. Deposita 49, 987–997. https://doi.org/10.1007/s00126-014-0554-z.

Migdisov, A., Williams-Jones, A.E., Brugger, J., Caporuscio, F.A., 2016. Hydrothermal transport, deposition, and fractionation of the REE: Experimental data and thermodynamic calculations. Chem. Geol. 439, 13–42. https://doi.org/10.1016/j.chemgeo.2016.06.005.

Milliken, R.E., Swayze, G.A., Arvidson, R.E., Bishop, J.L., Clark, R.N., Ehlmann, B.L., Green, R.O., Grotzinger, J.P., Morris, R.V., Murchie, S.L., Mustard, J.F., 2008. Opaline silica in young deposits on Mars. Geology 36, 847–850. https://doi.org/10.1130/G24967A.1.

Möller, P., 2000. Rare earth elements and Yttrium as geochemical indicators of the source of mineral and thermal waters. In: Stober, I., Bucher, K. (Eds.), Hydrogeology of Crystalline Rocks. Water Science and Technology Library. vol 34. Springer, Dordrecht. https://doi.org/10.1007/978-94-017-1816-5_10.

Mountain, B.W., Benning, L.G., Boerema, J.A., 2003. Experimental studies on New Zealand hot spring sinters: rates of growth and textural development. Can. J. Earth Sci. 40, 1643–1667. https://doi.org/10.1139/e03-068.

Muffler, L.J.P., White, D.E., Beeson, M.H., Truesdall, A.H., 1982. Geologic map of Upper Geyser Basin, Yellowstone National Park, Wyoming. U.S. Geological Survey Miscellaneous Investigations Map I-1371. scale 1:4,800 http://pubs.er.usgs.gov/publication/i1371.

Munoz-Saez, C., Saltiel, S., Manga, M., Nguyen, C., Gonnermann, H., 2016. Physical and hydraulic properties of modern sinter deposits: El Tatio Atacama. J. Volcanol. Geotherm. Res. 325, 156–168. https://doi.org/10.1016/j.jvolgeores.2016.06.026.

Nicholson, K., 1989. Early Devonian geothermal systems in Northeast Scotland: Exploration targets for epithermal gold. Geology 17, 568–571. https://doi.org/10.1130/0091-7613(1989)017<0568:EDGSIN>2.3.CO;2.

Nicolau, C., Reich, M., Lynne, B., 2014. Physico-chemical and environmental controls on siliceous sinter formation at the high-altitude El Tatio geothermal field, Chile. J. Volcanol. Geotherm. Res. 282, 60–76. https://doi.org/10.1016/j.jvolgeores.2014.06.012.

Pang, Z.H., Reed, M., 1998. Theoretical chemical thermometry on geothermal waters: problems and methods. Geochim. Cosmochim. Acta 62, 1083–1091. https://doi.org/10.1016/S0016-7037(98)00037-4.

Parker, R.J., Nicholson, K., 1990. Arsenic in geothermal sinters: determination and implications for mineral exploration. 12th NZ Geothermal Workshop. Auckland University, Auckland , pp. 35–39.. https://pangea.stanford.edu/ERE/pdf/IGAstandard/NZGW/1990/Parker.pdf.

Payne, C.E., 2016. Isotope Geochemistry of Gallium in Hydrothermal Systems. M.Sc. Thesis. Victoria University of Wellington. http://hdl.handle.net/10063/5554.

Phoenix, V., Renaut, R., Jones, B., Grant, F., 2005. Bacterial S-layer preservation and rare arsenic – antimony – sulphide bioimmobilization in siliceous sediments from Champagne Pool hot spring, Waiotapu, New Zealand. J. Geol. Soc. Lond. 162, 323–331. https://doi.org/10.1144/0016-764903-058.

Pirajno, F., 2020. Subaerial hot springs and near-surface hydrothermal mineral systems past and present, and possible extraterrestrial analogues. Geosci. Front. 11, 1549–1569. https://doi.org/10.1016/j.gsf.2020.04.001.

Planer-Friedrich, B., Forberg, J., Lohmayer, R., Kerl, C.F., Boeing, F., Kaasalainen, H., Stefánsson, A., 2020. Relative Abundance of Thiolated Species of As, Mo, W, and Sb in Hot Springs of Yellowstone National Park and Iceland. Environ. Sci. Technol. 54, 4295–4304. https://doi.org/10.1021/acs.est.0c00668.

Pokrovsky, O.S., Pokrovski, G.S., Schott, J., Galy, A., 2006. Experimental study of germanium adsorption on goethite and germanium coprecipitation with iron hydroxide: X-ray absorption fine structure and macroscopic characterization. Geochim. Cosmochim. Acta 70, 3325–3341. https://doi.org/10.1016/j.gca.2006.04.012.

Pope, J.G., Brown, K.L., McConchie, D.M., 2005. Gold concentrations in springs at Waiotapu, New Zealand: Implications for precious metal deposition in geothermal systems. Econ. Geol. 100, 677–687. https://doi.org/10.2113/gsecongeo.100.4.677.

Rapin, W., Chauviré, B., Gabriel, T.S.J., McAdam, A.C., Ehlmann, B.L., Hardgrove, C., Meslin, P.Y., Rondeau, B., Dehouck, E., Franz, H.B., Mangold, N., 2018. In situ analysis of opal in Gale Crater, Mars. J. Geophys. Res. 123, 1955–1972. https://doi.org/10.1029/2017JE005483.

Rodgers, K.A., Browne, P.R.L., Buddle, T.F., Cook, K.L., Greatrex, R.A., Hampton, W.A., Herdianita, N.R., Holland, G.R., Lynne, B.Y., Martin, R., Newton, Z., Pastars, D., Sannazarro, K.L., Teece, C.I.A., 2004. Silica phases in sinter's and residues from geothermal fields of New Zealand. Earth Sci. Rev. 66, 1–61. https://doi.org/10.1016/j.earscirev.2003.10.001.

Rouxel, O.J., Luais, B., 2017. Germanium isotope geochemistry. Rev. Mineral. Geochem. 82, 601–656. https://doi.org/10.2138/rmg.2017.82.14.

Ruff, S.W., Farmer, J.D., 2016. Silica deposits on Mars with features resembling hot spring biosignatures at El Tatio in Chile. Nat. Commun. 7, 1–10. https://doi.org/10.1038/ncomms13554.

Sanchez-Garcia, L., Fernandez-Martinez, M.A., García-Villadangos, M., Blanco, Y., Cady, S.L., Hinman, N., Bowden, M.E., Pointing, S.B., Lee, K.C., Warren-Rhodes, K., Lacap-Bugler, D., 2019. Microbial biomarker transition in high-altitude sinter mounds from El Tatio (Chile) through different stages of hydrothermal activity. Front. Microbiol. 9, 3350. https://doi.org/10.3389/fmicb.2018.03350.

Sanchez-Yanez, C., Reich, M., Leisen, M., Morata, D., Barra, F., 2017. Geochemistry of metals and metalloids in siliceous sinter deposits: Implications for elemental partitioning into silica phases. Appl. Geochem. 80, 112–133. https://doi.org/10.1016/j.apgeochem.2017.03.008.

Schulz, K.J., DeYoung Jr., J.H., Seal II, R.R., Bradley, D.C., 2017. Critical mineral resources of the United States—Economic and environmental geology and prospects for future supply: U.S. Geol. Surv. Prof. Pap. 1802, 797. https://doi.org/10.3133/pp1802.

Shanks III, W.C., Alt, J.C., Morgan, L.A., 2007. Geochemistry of sublacustrine hydrothermal deposits in Yellowstone Lake—Hydrothermal Reactions, Stable-Isotope Systematics, Sinter Deposition, and Spire Formation. U.S. Geol. Surv. Prof. Pap. 1717, 1–33.. https://pubs.usgs.gov/pp/1717/downloads/pdf/p1717G.pdf.

Sillitoe, R.H., 2015. Epithermal paleosurfaces. Mineral. Deposita 50, 767–793. https://doi.org/10.1007/s00126-015-0614-z.

Simmons, S.F., Brown, K.L., Tutolo, B.M., 2016. Hydrothermal transport of Ag, Au, Cu, Pb, Te, Zn, and other metals and metalloids in New Zealand geothermal systems: Spatial patterns, fluid-mineral equilibria, and implications for epithermal mineralization. Econ. Geol. 111, 589–618. https://doi.org/10.2113/econgeo.111.3.589.

Skok, J.R., Mustard, J.F., Ehlmann, B.L., Milliken, R.E., Murchie, S.L., 2010. Silica deposits in the Nili Patera caldera on the Syrtis Major volcanic complex on Mars. Nat. Geosci. 3, 838–841. https://doi.org/10.1038/ngeo990.

Smith, I.J., Lynne, B.Y., Jaworowski, C., Qasim, I., Heasler, H., Foley, D., 2018. The formation of geyser eggs at Old Faithful Geyser, Yellowstone National Park, U.S.A. Geothermics 75, 105–121. https://doi.org/10.1016/j.geothermics.2018.04.006.

Squyres, S.W., Arvidson, R.E., Ruff, S., Gellert, R., Morris, R.V., Ming, D.W., Crumpler, L., Farmer, J.D., Des Marais, D.J., Yen, A., McLennan, S.M., 2008. Detection of silica-rich deposits on Mars. Science 320, 1063–1067. https://doi.org/10.1126/science.1155429.

Sriaporn, C., Campbell, K.A., Millan, M., Ruff, S.W., Van Kranendonk, M.J., Handley, K.M., 2020. Stromatolitic digitate sinters form under wide-ranging physicochemical conditions with diverse hot spring microbial communities. Geobiology 18, 619–640. https://doi.org/10.1111/gbi.12395.

Tobler, D.J., Stefansson, A., Benning, L.G., 2008. In-situ grown silica sinters in Icelandic geothermal areas. Geobiology 6, 481–502. https://doi.org/10.1111/j.1472-4669.2008.00179.x.

Urrutia, M.M., Beveridge, T.J., 1994. Formation of fine-grained metal and silicate precipitates on a bacterial surface (Bacillus subtilis). Chem. Geol. 116, 261–280. https://doi.org/10.1016/0009-2541(94)90018-3.

Uysal, I.T., Gasparon, M., Bolhar, R., Zhao, J.X., Feng, Y.X., Jones, G., 2011. Trace element composition of near-surface silica deposits—a powerful tool for detecting hydrothermal mineral and energy resources. Chem. Geol. 280, 154–169. https://doi.org/10.1016/j.chemgeo.2010.11.005.

Van Kranendonk, M.J., Baumgartner, R., Djokic, T., Ota, T., Steller, L., Garbe, U., Nakamura, E., 2021a. Elements for the origin of life on land: a deep-time perspective from the Pilbara Craton of Western Australia. Astrobiology 21, 39–59. https://doi.org/10.1089/ast.2019.2107.

Van Kranendonk, M., Baumgartner, R., Cady, S., Campbell, K., Damer, B., Deamer, D., Djokic, T., Gangidine, A., Ruff, S., Walter, M.R., 2021b. Terrestrial hydrothermal fields and the search for life in the Solar System. Bull. Am. Astron. Soc. 53, 272. https://doi.org/10.3847/25c2cfeb.a3a646ab.

Walter, M.R., 1976. Geyserites of Yellowstone National Park: an example of Abiogenic "Stromatolites". Developments in Sedimentology. 20, pp. 87–112. https://doi.org/10.1016/S0070-4571(08)71131-2.

White, S.J.O., Shine, J.P., 2016. Exposure potential and health impacts of indium and gallium, metals critical to emerging electronics and energy technologies. Curr. Environ. Health Rep. 3, 459–467. https://doi.org/10.1007/s40572-016-0118-8.

White, N.C., Wood, D.G., Lee, M.C., 1989. Epithermal sinters of Paleozoic age in North Queensland, Australia. Geology 17, 718–722. https://doi.org/10.1130/0091-7613(1989)017<0718:ESOPAI>2.3.CO;2.

White, D.E., Heropoulos, C., Fournier, R.O., 1992. Gold and Other Minor Elements Associated with the Hot Springs and Geysers of Yellowstone National Park, Wyoming, Supplemented with Data from Steamboat Springs, Nevada, U.S. Geological Survey Bulletin, 2001. https://doi.org/10.3133/b2001.

Wood, S.A., Samson, I.M., 2006. The aqueous geochemistry of gallium, germanium, indium and scandium. Ore Geol. Rev. 28, 57–102. https://doi.org/10.1016/j.oregeorev.2003.06.002.

Zhai, D., Mathur, R., Liu, S.A., Liu, J., Godfrey, L., Wang, K., Xu, J., Vervoort, J., 2021. Antimony isotope fractionation in hydrothermal systems. Geochim. Cosmochim. Acta 306, 84–97. https://doi.org/10.1016/j.gca.2021.05.031.

Zhou, B., Ren, E., Sherriff, B.L., Yao, Y., 2013. Multinuclear NMR study of Cs-bearing geyserites of the Targejia hot spring cesium deposit in Tibet. Am. Mineral. 98, 907–913. https://doi.org/10.2138/am.2013.4273.